J. Fluid Mech. (2025), *vol.* 1022, A2, doi:10.1017/jfm.2025.10756

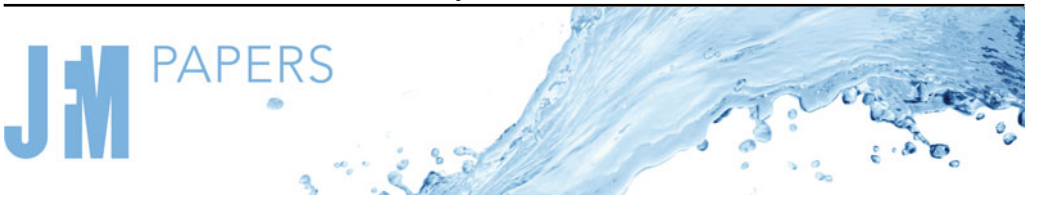

Incomplete similarity of the turbulent boundary layer over an aerofoil in the presence of synthetic jets

Ali Shirinzad[1], **Kecheng Xu**[2], **Mojtaba Kheiri**[3] and **Pierre Edward Sullivan**[1]

[1]Department of Mechanical and Industrial Engineering, University of Toronto, Toronto, ON M5S 3G8, Canada

[2]University of Toronto Institute for Aerospace Studies, Toronto, ON M3H 5T6, Canada

[3]Department of Mechanical, Industrial and Aerospace Engineering, Concordia University, Montréal, PQ H3G 1M8, Canada

Corresponding author: Ali Shirinzad, ali.shirinzad@mail.utoronto.ca

(Received 13 April 2025; revised 8 September 2025; accepted 21 September 2025)

This study is concerned with the near-wall flow structure over a NACA 0025 aerofoil at a constant chord-based Reynolds number of 100 000 across various angles of attack, where an array of 12 circular-orifice synthetic jet actuators (SJAs) was used to reattach the flow under conditions of flow separation. The SJAs were operated in burst-mode at two distinct momentum coefficients, a 50 % duty cycle and a modulation frequency of 200 Hz, targeting the separated shear layer frequency. Particle image velocimetry was conducted using three side-by-side cameras to capture the velocity fields along the aerofoil surface at the centreline. At zero angle of attack, the velocity profiles exhibited characteristics of a turbulent boundary layer, following the law of the wall in the inner layer while deviating from the logarithmic law in the outer layer. At higher angles of attack, while some logarithmic behaviour could still be detected close to the wall, a wide region of the velocity profiles became predominantly linear, exhibiting a behaviour differing from both a canonical turbulent boundary layer and a turbulent wall jet. The entire shear flow was decomposed into three regions: the boundary layer, the jet layer and the mixing layer that extended between the two. The mixing layer was analysed by applying several scaling laws to the time-averaged velocity components, where it was revealed that the characteristic velocity of the two velocity components is different. An asymptotic solution was obtained under a low spreading rate at infinite Reynolds number, providing a theoretical basis for the experimental observations.

Key words: turbulent boundary layers, boundary layer control, free shear layers

1. Introduction

Flow separation is generally defined as the breakaway or detachment of fluid from a bounding surface, caused by an adverse pressure gradient, a geometrical aberration or other means (Gad-el Hak & Bushnell 1991). Flow separation is marked by an increase in the normal velocity component and an abrupt thickening of the rotational flow region adjacent to the surface (Gad-el Hak & Bushnell 1991). In many engineering applications, flow separation is undesirable as it can lead to reduced lift, increased drag, elevated noise levels and potential structural vibrations. This issue is particularly relevant in applications involving aerofoils, such as low-pressure turbine blades, micro air vehicles and unmanned aerial vehicles (Hodson & Howell 2005; Shkarayev *et al.* 2007; Yang & Hu 2008; Savaliya, Kumar & Mittal 2010). Hence, separation control, now part of the broader field of flow control, has been a key research focus for over a century. Flatt (1961) defined the term boundary layer control as any mechanism or process that alters the natural behaviour of the boundary layer. A more general definition for flow control was presented by Gad-el Hak (2000) as any attempt to drive the character or disposition of a flow field to a more favourable one. Flow control devices are classified as either passive or active. Passive devices, such as vortex generators, delay flow separation without requiring external energy input. In contrast, active flow control devices rely on an external power source. Among active methods, fluidic jets have been extensively studied and implemented, with various forms, including steady, pulsed, synthetic and plasma jets, used to inject momentum into a retarded boundary layer. The present work focuses specifically on boundary layer control over an aerofoil using synthetic jets, which will be addressed in detail in the following sections. Given the historical precedence of steady jets in boundary layer control and their conceptual relevance to synthetic jets, the authors deem it necessary to provide a brief review of their key features as a precursor to the discussion on synthetic jets.

1.1. *The turbulent wall jet*

A shear layer is a thin region of flow characterised by a significant tangential velocity gradient. Both boundary layers and jets fall under the category of shear flows: the former develops near a solid surface due to frictional forces, while the latter emerges when a high-momentum fluid stream exits a nozzle, aperture or an orifice into a surrounding medium. A common analytical approach involves order-of-magnitude estimates to approximate the governing equations, enabling the derivation of analytical solutions within a limited scope. In the study of semibounded and free shear layers, assessing whether the flow exhibits self-preserving behaviour is of both fundamental and practical interest. Self-similar solutions provide insight into the intermediate asymptotic behaviour of a broader class of flow phenomena (Gratton 1991). Additionally, these solutions help minimise the need for extensive experiments or simulations and serve as benchmarks for validating experimental or numerical data (Djenidi & Agrawal 2024).

A turbulent round jet issued into a quiescent environment becomes self-preserving a few diameters downstream of the nozzle at high Reynolds numbers (Wygnanski & Fiedler 1969). In this self-similar state, the jet grows linearly at a constant spreading rate, which is generally considered independent of the jet Reynolds number (Rodi 1975; Panchapakesan & Lumley 1993; Hussein, Capp & George 1994). Turbulent jets can generate supercirculation on lifting surfaces, aiding in applications such as separation control over slotted flaps (Neuendorf & Wygnanski 1999). The flow field due to a turbulent jet along a wall is no longer a simple boundary layer but rather a hybrid of a free jet and a boundary layer, known as a wall jet. The term wall jet was first used by Glauert (1956) who studied the evolution of a two-dimensional jet exiting a wide nozzle along a

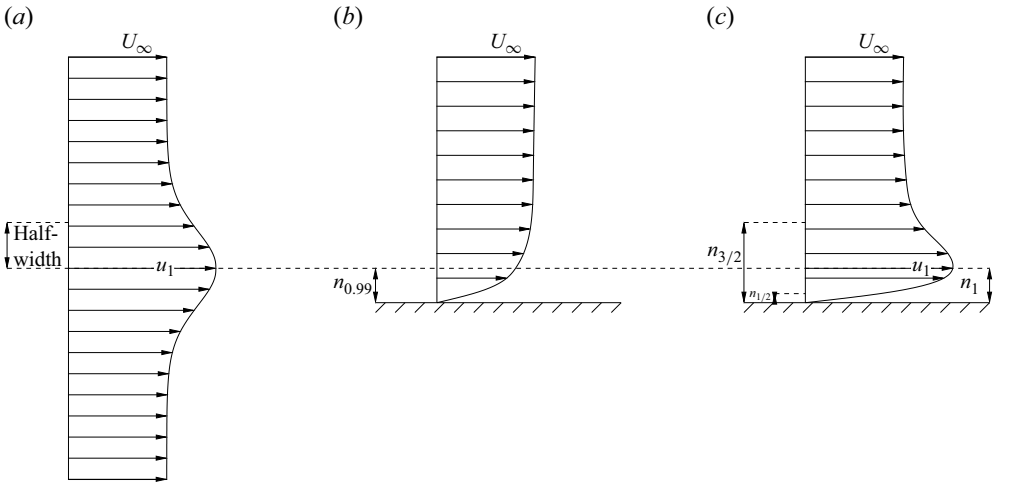

Figure 1. A schematic drawing showcasing the encountered tangential velocity profiles for (*a*) a turbulent free jet, (*b*) a turbulent boundary layer and (*c*) a turbulent wall jet.

flat plate. Launder & Rodi (1983) defined a wall jet as a shear flow directed along a wall where, by virtue of the initially supplied momentum, at any station, the streamwise velocity over some region within the shear flow exceeds that of the free stream. The injection of high-momentum fluid along the wall creates two shear layers that strongly interact with each other as they grow in the streamwise direction. Typical profiles of the time-averaged tangential velocity $\overline{u}$ for a free jet, a boundary layer and a wall jet are shown in figure 1. The half-width of a free jet is defined as the normal distance from the jet centreline to the location where $\overline{u} = (u_1 + U_\infty)/2$. For a turbulent wall jet, n_1 represents the normal distance from the wall to the point of maximum mean velocity. Similarly, the lengths $n_{3/2}$ and $n_{1/2}$ are defined as the normal distances to the locations where $\overline{u} = (u_1 + U_\infty)/2$ and $\overline{u} = u_1/2$, analogous to the half-width of a free jet.

A complete self-similarity in a semibounded flow, such as a turbulent boundary layer or a turbulent wall jet, is not expected due to the different characteristic scales in the inner and outer regions (Glauert 1956; Wygnanski, Katz & Horev 1992). In a turbulent boundary layer, the gross characteristics of the turbulence in the outer layer resemble those of a free shear flow, with the mean tangential velocity $\overline{u}$ following the velocity defect law (von Kármán 1930). In contrast, the inner region is governed solely by viscous scales (Prandtl 1925). At sufficiently high Reynolds numbers, there is an overlap between the inner and outer layers, leading to the emergence of the logarithmic law of the wall (von Kármán 1930; Millikan 1938). It is established that the outer layer may be described by power laws in the limit of an infinite Reynolds number (Barenblatt 1993). A turbulent wall jet exhibits characteristics of both a turbulent boundary layer and a free jet (Dakos, Verriopoulos & Gibson 1984). Near the wall, the law of the wall generally applies, though the constants in the logarithmic law may differ from those observed in turbulent boundary layers (Banyassady & Piomelli 2014). The profile is conventionally divided into the inner and outer layers as the regions below and above the maximum velocity location, respectively. These two layers are alternatively referred to as the boundary layer and the jet layer. The inner layer may be scaled similarly to a turbulent boundary layer, using the friction velocity and maximum velocity position n_1 as the characteristic velocity and length scales, whereas the outer layer scaling is similar to a free jet (Wygnanski *et al.* 1992). Still, Gee & Bradshaw (1960) argued that the defect law for the inner layer of the

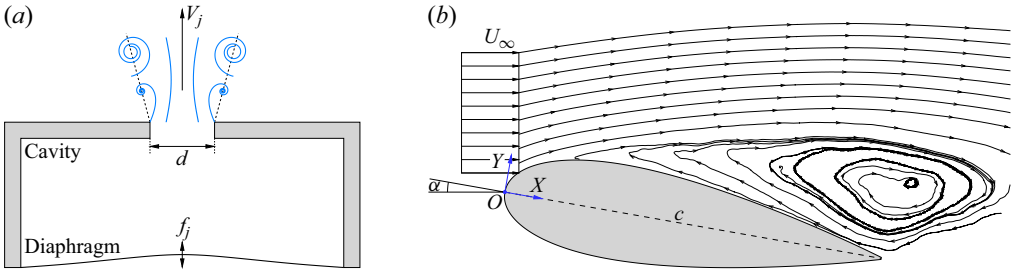

Figure 2. Schematic representations and pertinent parameters for (*a*) a SJA and (*b*) flow over an aerofoil.

turbulent wall jet is no longer the simple form proposed by von Kármán (1930). George *et al.* (2000) proposed power-law solutions for both inner and outer layers in the limit of an infinite Reynolds number. However, the power-law exponents are not definitive for finite Reynolds numbers (Banyassady & Piomelli 2014; Naqavi, Tyacke & Tucker 2018). Currently, no broad consensus exists on the scaling approach for the Reynolds stresses (George *et al.* 2000; Hao & di Mare 2023; Djenidi & Agrawal 2024).

In a turbulent wall jet, the point of zero Reynolds shear stress no longer coincides with the position of the zero velocity gradient and instead lies closer to the wall due to the interaction of the inner and outer shear layers. A qualitative explanation based on the memory of turbulent structures is that, since the streamlines intersect with the location of the maximum velocity, they convey the properties of the outer layer into the inner layer (Alcaraz, Charnay & Mathieu 1977). Wall jets flowing along convex surfaces have a tendency to adhere to the nearby wall, a phenomenon commonly referred to as the Coanda effect (Danon, Gregory & Greenblatt 2016). The Coanda cylinder, which is a two-dimensional circular cylinder, is the most common set-up used to study the development of wall jets over convex surfaces. Based on the inviscid stability criterion (Rayleigh 1916), a curved wall jet may undergo centrifugal instability (Joshi & Tumin 2004). Experimental observations and flow visualisations have confirmed the presence of streamwise vortices due to centrifugal instability (Likhachev, Neuendorf & Wygnanski 2001; Cullen *et al.* 2002; Joshi & Tumin 2004), which are also believed to be the reason for the wall jet to spread outward to a greater extent compared with a flat surface (Alcaraz *et al.* 1977; Neuendorf & Wygnanski 1999). For convex surfaces, the position of zero shear stress moves farther from the position of the maximum velocity compared with a flat plate. In general, a convex curvature has a stabilising effect on the turbulent intensities in the inner layer and a destabilising effect in the outer layer (Alcaraz *et al.* 1977; Dakos *et al.* 1984).

1.2. *The interaction of synthetic jets with the cross-flow over an aerofoil*

A synthetic jet actuator (SJA) is a fluidic device typically consisting of a vibrating diaphragm or piston that alters the fluid volume within a cavity to eject a quasisteady jet through a nozzle, aperture or an orifice. The periodic oscillation of the actuator leads to a cycle of ingestion and expulsion of the working fluid. If the momentum of the fluid exiting the aperture is high enough to escape the suction cycle, a synthetic jet is formed that propagates away from the origin (Glezer & Amitay 2002). A schematic representation of an SJA is presented in figure 2(*a*), where f_j is the diaphragm excitation frequency, d is the aperture width or diameter and V_j is the time-averaged jet centreline velocity at the exit. Synthetic jets are sometimes referred to as zero-net mass-flux jets as

they are formed entirely from the working fluid within the flow system where they are employed.

The flow field of a synthetic jet in quiescent conditions is generally divided into three regions: the near, transitional and far-field. The transitional region is typically ignored for simplicity (Smith & Glezer 1998; Cater & Soria 2002). The near-field region is dominated by the time-periodic formation and advection of the vortex structures (Smith & Glezer 1997, 1998). Hence, the flow characteristics differ from that of a steady jet that has negligible temporal variations. In fact, periodic forcing provided by SJAs has been observed to offer greater entrainment of ambient fluid in the near-field compared with steady jets (Smith & Swift 2001; Cater & Soria 2002). Experiments have confirmed that the far-field behaviour of synthetic jets is comparable to steady jets, and the time-averaged velocity eventually becomes self-similar, although with a higher spreading rate and decay constant due to the increased entrainment in the near-field (Smith & Swift 2001; Cater & Soria 2002; Shuster & Smith 2007).

There is a relatively extensive body of work on the use of synthetic jets for separation control over an aerofoil. This surge in research interest is partially due to the unique features of SJAs, primarily no requirement for external fluid supply or ducting that significantly reduces the mechanical complexity and weight of the flow control system (Glezer & Amitay 2002; Zhong *et al.* 2007). Another reason is the complex interactions of synthetic jets with the cross-flow over an aerofoil, which depend on a large number of geometrical and operational parameters. Consider the flow over an aerofoil, as shown in figure 2(*b*), where (X, Y) are the global coordinates, α is the angle of attack, c is the chord length and U_∞ is the free stream velocity. The chord-based Reynolds number is defined as $Re_c = U_\infty c/\nu$, where ν is the fluid kinematic viscosity. Depending on the angle of attack α and Reynolds number Re_c, three flow regimes are observed: fully attached flow, separated and reattached flow and separated flow (Winslow *et al.* 2018). Compared with the Reynolds number Re_c, the angle of attack α has a similar but inverse effect on the state of the flow (Yang & Hu 2008; Winslow *et al.* 2018). A comprehensive summary of the flow phenomenon for Reynolds numbers ranging from 1000 to 200 000 is reported by Carmichael (1981). Generally, when the Reynolds number decreases below 10^6, particularly if $Re_c < 50\,000$, separation may occur near the leading edge of the aerofoil (Carmichael 1981; Lissaman 1983). If the Reynolds number is sufficiently low, the separated shear layer fails to reattach to the aerofoil surface, forming a wide turbulent wake. Over an intermediate range, the turbulent separated shear layer may reattach to the aerofoil surface and form a laminar separation bubble.

Synthetic jet actuators have been found to be most effective when the actuation frequency f_j is set to a value close to an instability frequency of the baseline flow (Greenblatt & Wygnanski 2000; Amitay & Glezer 2002*b*). This principle was reinforced by the direct numerical simulations of Palumbo *et al.* (2022), who conducted a parametric study over a range of actuation frequencies for a flat plate. Their results showed that the control authority of an SJA, in terms of promoting early transition, does not increase monotonically with frequency. Instead, optimal performance is achieved when f_j is near the frequency of the most spatially amplified Tollmien–Schlichting wave. For an aerofoil, the SJA forcing frequency is normalised as $f^* = f_j c/U_\infty$, called the reduced frequency. The value of the reduced frequency may be set to $f^* \sim O(1)$ or $f^* \sim O(10)$, corresponding to the wake and separated shear layer frequencies, respectively. Both cases have been shown to be effective in restoring aerodynamic performance. However, forcing at $f^* \sim O(1)$ results in unsteady reattachment, whereas forcing at $f^* \sim O(10)$, which is decoupled from the unsteady baseline frequencies, leads to the damping of global flow oscillations (Amitay & Glezer 2002*b*; Glezer, Amitay & Honohan 2005). The interaction

of high-frequency synthetic jets with a cross-flow leads to a local modification of the apparent aerodynamic shape, often referred to as the virtual aeroshaping effect.

Synthetic jet actuators should ideally be operated at an optimal frequency, typically identified under quiescent conditions, which maximises the momentum output. However, targeting the natural flow instabilities may require the SJAs to operate at a suboptimal excitation frequency. A solution proposed by Amitay & Glezer (2002*a*) is to use burst modulation, allowing the SJA to be driven at a carrier frequency that maximises momentum, while the modulation frequency f_j is used to specifically target the desired flow instabilities. The initiation of actuation over a convex surface is known to cause a Coanda-like attachment of the separated shear layer (Amitay & Glezer 2002*a*), a similar behaviour to that of the wall jets. According to Greenblatt & Wygnanski (2000), curvature does not have a significant effect on the optimum reduced frequencies for separation control.

Another crucial factor in flow control effectiveness is the strength of the synthetic jets with respect to the cross-flow, which is often characterised by the blowing ratio $C_b = V_j/U_\infty$ or the momentum coefficient C_μ. The blowing ratio is simply defined as the ratio of the time-averaged jet centreline velocity to the free stream velocity. The momentum coefficient C_μ is generally defined as the ratio of the time-averaged expelled momentum by the operating SJA to the momentum of the free stream. While both of these parameters are frequently used by researchers, the momentum coefficient C_μ may be more appropriate for finite-span SJAs as it also accounts for the difference between the total jet area and the reference cross-flow area, though the exact mathematical definition of C_μ is not consistent in the literature (Greenblatt & Wygnanski 2000; Glezer *et al.* 2005; Sahni *et al.* 2011). Overall, the existing works show that there is a lower threshold for the momentum coefficient C_μ, below which actuation is essentially ineffective as the jets do not have enough momentum to penetrate the cross-flow (Goodfellow, Yarusevych & Sullivan 2013).

1.3. *Objectives*

The interaction of synthetic jets and the cross-flow over an aerofoil has been a subject of research for several decades, with numerous studies examining the near-field region, the formation and advection of flow structures and the influence of geometric and operational parameters on separation control. Of particular interest are the similarities between synthetic jets and conventional steady jets in the far-field region. While these similarities have been explored for synthetic jets in quiescent conditions, as discussed in § 1.2, an intriguing question remains: Does the far-field region of this flow have any resemblance to a turbulent wall jet over a convex surface? If so, can it be scaled similarly, perhaps using the scaling laws described in § 1.1? The objective of this study is to address these questions and provide deeper insight into the far-field behaviour of these flows. The remainder of the paper is organised as follows: the experimental set-up, methodology and postprocessing procedure are described in § 2; the main results and discussion are presented in § 3; the major findings and conclusions are summarised in § 4.

2. Experimental procedure

2.1. *Wind tunnel facility*

The experiments were conducted in a closed return low-speed wind tunnel located in the Turbulence Research Laboratory at the Department of Mechanical and Industrial Engineering, University of Toronto. A schematic showing the main components of the

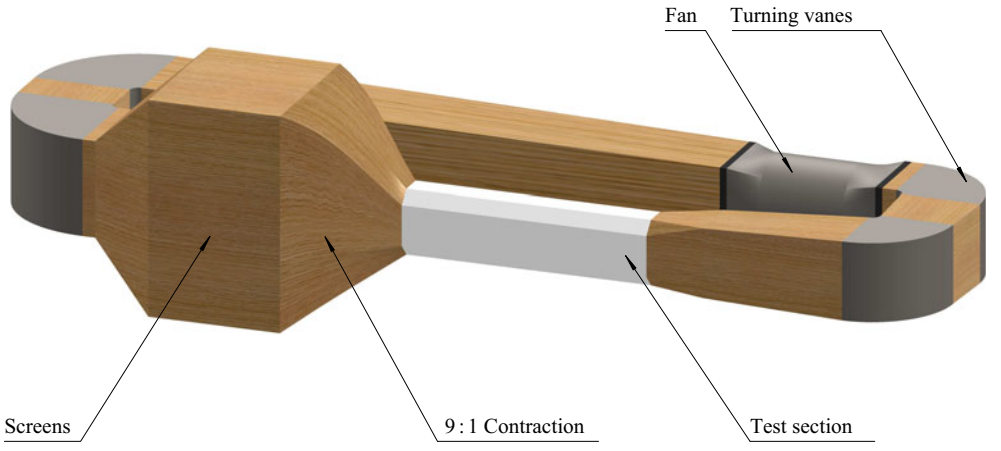

Figure 3. A schematic showing the various components of the wind tunnel facility.

wind tunnel facility is shown in figure 3. The test section of the wind tunnel is 5000 mm long with an octagonal cross-section 1220 mm high and 910 mm wide. The corners of the octagonal cross-section have a constant angle but decrease in width along the test section length to increase the cross-sectional area and compensate for boundary layer growth. The ceiling and one of the sidewalls of the test section are fabricated from clear acrylic plates to facilitate optical access. The flow in the tunnel is driven by a six-bladed axial fan, powered by a REEVES MotoDrive 500 series motor located outside the wind tunnel on an isolating concrete pad. The fan housing is connected to the wind tunnel by flexible couplings to minimise the transfer of vibrations from the fan to the tunnel structure. The free stream velocity in the test section is adjustable from 2.5 to 18.0 $\mathrm{m\,s^{-1}}$, monitored using a Pitot-static tube installed at the test section inlet with an uncertainty estimated to be less than $\pm 1\,\%$. The flow entering the test section passes through a conditioning unit consisting of seven screens and a 9 : 1 converging section to minimise the turbulence and homogenise the flow. The free stream is mostly uniform with a turbulence intensity generally less than 0.1 %. The flow exiting the test section is redirected by four 90° corners of the wind tunnel through a turning vane system for flow recirculation.

2.2. *Aerofoil model and instrumentation*

The aerofoil model used in the present study is a NACA 0025 profile with an open trailing edge. The aerofoil model, machined from aluminium, has a chord length of $c = 300$ mm and a spanwise extent of 885 mm. The selection of the NACA 0025 profile was primarily driven by geometric constraints associated with integrating the SJA array near the leading edge. Approximately one third of the middle section of the model is hollow to permit the installation of the SJAs and pressure sensors. The model was fitted with two circular acrylic end plates to suppress edge effects. The end plates were fixed to the ends of the model and positioned 15 mm from the tunnel walls to isolate the model from the tunnel sidewall boundary layers. There was no gap between the model and the end plates. It has been verified experimentally that end effects do not influence flow development over at least 50 % of the aerofoil span within the domain of interest (Yarusevych, Sullivan & Kawall 2009). The model with the attached end plates was installed 400 mm downstream of the entrance to the test section. A rotation lock and bearing housings attached to the end plates were used to adjust the pitch angle of the aerofoil. A digital protractor was employed to adjust the angle of attack to the desired values with an uncertainty

of $\pm 0.1°$. The aerofoil model was equipped with 64 pressure taps, each 0.8 mm in diameter, which were located at the aerofoil centreline and were connected to a Scanivalve pressure scanner through pneumatic tubing. The pressure could then be measured by an MKS Baratron 226A pressure transducer, with a range of ± 26.66 Pa, in conjunction with the Scanivalve pressure scanner. The maximum uncertainty associated with the surface pressure measurements is ± 2 %. The aerofoil was sprayed black to minimise reflection, and no further antireflection material could be applied due to the presence of the pressure taps.

An array of 24 Murata MZB1001T02 microblowers was mounted near the leading edge, housed within a rectangular cavity measuring 317 mm in width and 58 mm in length, located inside the hollow section of the aerofoil. The microblowers were arranged symmetrically about the aerofoil centreline in two equal rows, with none positioned directly on the centreline. The upstream row of the array was located at $X_j/c = 0.1$ in the vicinity of the separation point. The SJA array was wired such that each row was powered independently. Only the upstream row was activated in the present study to investigate the flow structures induced by a single actuator array, without the added complexity of interactions between multiple synthetic jets. Each SJA had a circular orifice of diameter $d = 0.8$ mm the centre of which was 25 mm apart from the centre of the nearest microblowers. The microblowers operational range was between 5 V to 30 V, capable of providing 24.0 kHz to 27.0 kHz of excitation frequency. Using a Rigol DG1022Z function generator, the microblowers were burst modulated at a carrier wave frequency of 25.5 kHz, a 50 % duty cycle and a modulation frequency of $f_j = 200$ Hz. The output signal was amplified by a YAMAHA HTR5470 amplifier to a peak-to-peak voltage within the microblower operational range.

2.3. *Velocity measurements*

The NACA 0025 aerofoil is symmetric and, consequently, the distribution of the time-averaged pressure coefficient on the suction and pressure sides are expected to be almost identical at a zero degree angle of attack. The free stream static pressure p_∞ was measured from the static side of the pitot tube used to measure the free stream velocity at the test section inlet. At each pressure port, a total of 30 000 samples were collected at a frequency of 1000 Hz to resolve the time-averaged surface pressure distribution along the aerofoil. The pressure coefficient was then obtained according to $C_p = (\overline{p} - p_\infty)/(0.5\rho U_\infty^2)$, where $\overline{p}$ is the time-averaged pressure and ρ is the air density. The results for the optimal position, used as the reference for angle of attack measurement, are plotted in figure 4.

The experiments involved eight controlled cases across four angles of attack and two momentum coefficients and the baseline case at zero angle of attack. The chord-based Reynolds number was set to $Re_c = 10^5$ throughout the entire experiment by adjusting the free stream velocity. The excitation frequency was also kept constant at $f_j = 200$ Hz to yield a reduced frequency of $f^* \sim O(10)$ over all cases, targeting the separated shear layer frequency. For the controlled cases, the investigated angles of attack were $\alpha = 0$, $7.5°$, $12.5°$ and $15.0°$, where the free stream velocity was $U_\infty = 5.22$ m s^{-1}, 5.22 m s^{-1}, 5.28 m s^{-1} and 5.28 m s^{-1}, respectively. These slight differences in the measured free stream velocity were due to variations in atmospheric pressure across the datasets. A measurement of the boundary layer profile on the tunnel wall at the location corresponding to the end plate leading edge showed that the boundary layer was 12 mm thick at $U_\infty = 5.20$ m s^{-1}. Hence, no significant interaction exists between the model and the tunnel sidewall boundary layer (Feero 2018). At each angle of attack, the peak-to-peak voltage of the input signal to the SJA array was set to two distinct values, $V_{pp} = 10$V

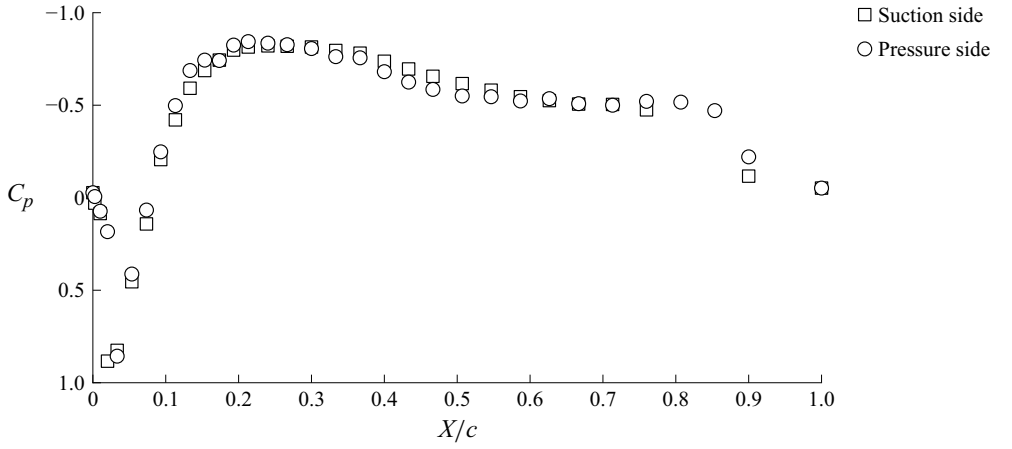

Figure 4. The mean pressure coefficient along the aerofoil at zero angle of attack.

and 20 V, corresponding to $C_\mu = 0.25 \times 10^{-3}$ and 1.25×10^{-3} (Xu 2025). At an angle of attack of $\alpha = 17.5°$, the separated flow could no longer be attached with the current settings. The baseline flow at $\alpha = 0$ was examined separately, and the free stream velocity for this case was 5.30 m s^{-1}. The Mach number for all test conditions was relatively low ($Ma \ll 0.3$) and, hence, the flow could be considered incompressible.

A two-dimensional two-component particle image velocimetry (PIV) system was employed to measure the instantaneous velocity fields at the spanwise centreline of the aerofoil model. The flow was seeded by a SAFEX 2010F fog generator with SAFEX-Inside-Nebelfluid, which is a mixture of diethylene glycol and water. A circular laser beam was generated by a Litron Bernoulli neodymium-doped yttrium aluminium garnet (Nd:YAG) laser capable of emitting green light up to a maximum pulse energy of 200 mJ per pulse at a wavelength of 532 nm. The laser beam was redirected over the test section ceiling, where it was spread into a light sheet by concave and convex THORLABS cylindrical lenses with a focal length of −13.7 and 1000 mm to illuminate the seeding particles. The laser light sheet had a thickness of approximately 1 mm, and was carefully aligned at the aerofoil centreline. Three 12-bit complementary metal oxide semiconductor JAI SP-5000M-USB cameras were fitted with Azure 7526ML12M 1.1" 75 mm lenses and positioned side-by-side to capture the far-field flow region spanning the range $0.35 \leqslant X/c < 1.03$, or $(X - X_j)/d > 93$ if normalised by the orifice diameter. All three cameras had a resolution of 2560 pixels × 2048 pixels, and a pixel density of 34.2 pixels mm^{-1} after calibration. The resulting fields of view for the three cameras were 75 mm long and 60 mm high, overlapping by 10 mm in the chordwise direction. A schematic showing the aerofoil model, SJA array and the PIV arrangements is provided in figure 5. The image acquisition was timed by an NI PCIe-6323 data acquisition card at a sampling frequency of 10 Hz to obtain statistically independent samples. Following Scharnowski, Bross & Kähler (2019), the time delay between the two frames in an image pair was set to 60 µs to obtain an appropriate in-plane particle displacement. For the controlled cases, the image recording was synchronised to the start of the actuation cycle to allow for phase-locked data acquisition. For each phase-locked case, starting at $\phi = 0°$ and ending with $\phi = 315°$ with an increment of $\phi = 45°$, 1000 image pairs were collected, resulting in a total of 8000 image pairs. For the baseline flow, 8000 image pairs were acquired without a particular reference event in the flow. The images from the three cameras were stitched using a linear combination of the intensities in the two overlapping regions. All images

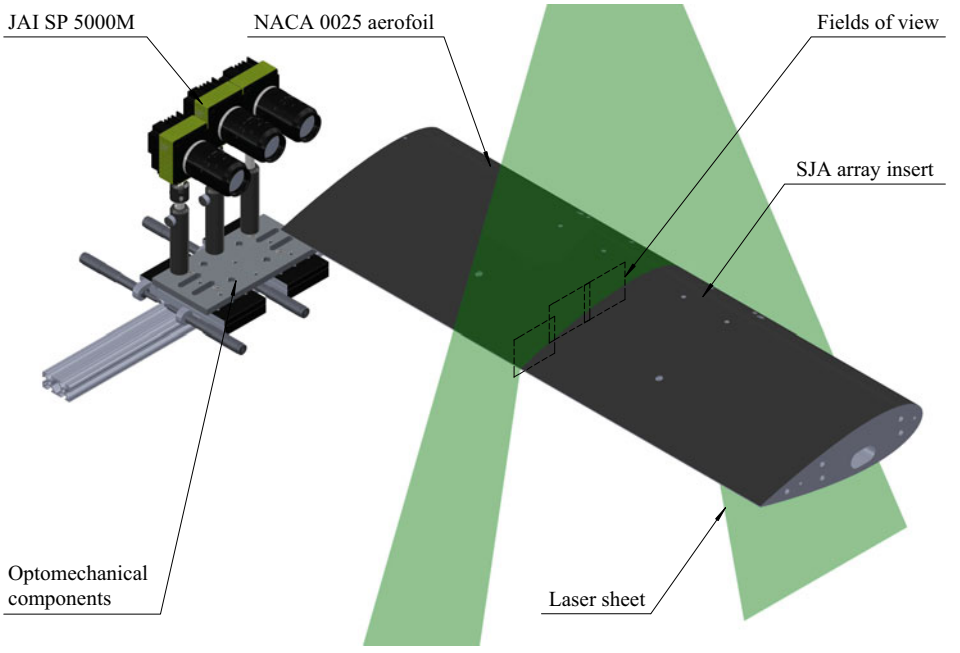

Figure 5. A schematic showing the aerofoil model, the three JAI cameras, the resulting fields of view and other optomechanical components.

were processed with the open-source software OpenPIV-Python-GPU, which utilises a window deformation iterative multigrid algorithm. The PIV process comprised of an initial iteration at a window size of 64 pixels $\times$ 64 pixels, two iterations at 32 pixels $\times$ 32 pixels and two iterations at a final window size of 16 pixels $\times$ 16 pixels. Median validation with a kernel size of three and a threshold of two was applied at every iteration to filter and replace the outliers. The percentage of outliers generally remained below 0.5 %. The resulting vector spacing was around 0.23 mm ($0.00078c$) for all test cases.

2.4. *Data postprocessing*

The PIV processing yields two velocity components in a local Cartesian coordinate system. The nature of this study demands the velocity to be decomposed in directions that are tangent and normal to the aerofoil surface. In this study, three coordinate systems are adopted: the global Cartesian coordinates (X, Y) already shown in figure 2(b), the local Cartesian coordinates (x, y, z) with its origin at the bottom left-hand corner of the captured field ($X_o/c = 0.35$), and the curvilinear coordinates (s, n, z) that use the aerofoil profile as its reference curve to locate any point in the measurement plane using the arclength s and the wall-normal distance n. The terminology, as well as the local Cartesian and curvilinear coordinate systems are shown in figure 6. The origin of the curvilinear coordinates lies on the y-axis, exactly on the surface of the aerofoil. The arclength s and surface curvature $\varrho = 1/r_0$ are measured using the open-trailing-edge NACA 0025 aerofoil profile. The three velocity components along the axes of each coordinate system are denoted by the corresponding axis as a subscript. The only exception is the tangential velocity, denoted by the subscript t instead of s. The velocities in the curvilinear coordinate system may then be obtained by transforming the measured velocities through the following relations:

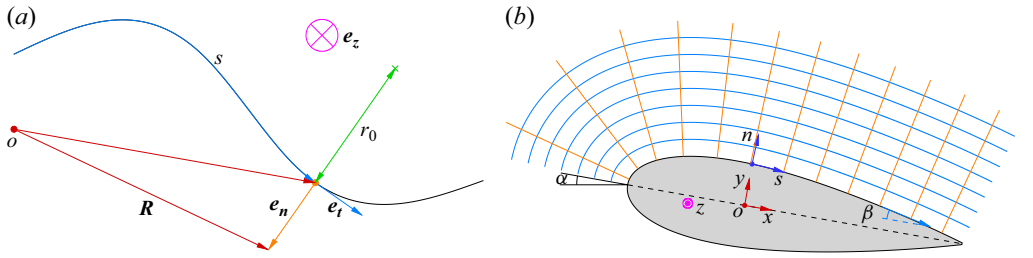

Figure 6. Schematics illustrating (*a*) Frenet–Serret frame for an arbitrary two-dimensional curve and (*b*) adopted coordinate systems for the NACA 0025 aerofoil, with the n- and s-contour lines designated in blue and orange colours, respectively.

$$u_t = u_x \cos(\beta) + v_y \sin(\beta), \tag{2.1}$$

$$v_n = v_y \cos(\beta) - u_x \sin(\beta), \tag{2.2}$$

where β is the slope of the surface with respect to the chord. Equations (2.1) and (2.2) are also applicable to the time- and phase-averaged velocities. We adopt the typical notations for the time-averaged, phase-averaged and fluctuating characteristics: $\overline{(\cdot)}$, $\langle\cdot\rangle$ and $(\cdot)'$. In addition to the symbols already defined in § 1, we use the following terminology for shear flow analyses. The mean tangential velocity on the wall is designated by u_0, where $u_0 = 0$ at finite Reynolds numbers and $u_0 \neq 0$ at infinite Reynolds number. For $0 \leqslant \varepsilon \leqslant 1$, we define the cross-stream location n_ε as the point where the mean tangential velocity reaches a value of $\overline{u_t} = (1-\varepsilon)u_0 + \varepsilon u_1$. The values at the cross-stream location n_ε are denoted by an ε subscript. All other symbols shall be defined explicitly. The post-processing, data analysis and visualisation were accomplished using MATLAB and the commercial software Origin.

3. Results and discussion

3.1. *The dissimilar scaling of the velocity*

In this section, we consider the applicability of the scaling laws discussed in § 1.1 to the mean velocities. For convenience, we non-dimensionalise the time-averaged velocities by the free stream velocity according to the following expressions:

$$u^* = \frac{\overline{u_t}}{U_\infty}, \qquad v^* = \frac{\overline{v_n}}{U_\infty}. \tag{3.1}$$

We begin by examining the near-wall flow region at zero angle of attack, which is expected to resemble a boundary layer as the synthetic jets are inactive. In this scenario, the mean velocity should follow the logarithmic law in the overlap region for sufficiently high Reynolds numbers. We define the characteristic thickness as $\delta \equiv n_{0.99}$, which aligns with the conventional boundary layer definition. Profiles of the dimensionless mean tangential velocity u^* for the baseline case are shown in figure 7, where the point at $n_{0.99}$ is marked by a closed symbol. Evidently, the profiles of u^* in this case closely resemble that of a turbulent boundary layer, with the semilogarithmic plots indicating the presence of a logarithmic region near the wall. Now, let us examine the profiles of u^* at $\alpha = 15.0°$ and $C_\mu = 1.25 \times 10^{-3}$, as shown in figure 8. In controlled cases, the tangential velocity profile may exhibit a peak near the wall, similar to turbulent wall jets. Nevertheless, we continue to use $\delta \equiv n_{0.99}$ instead of n_1 for our analyses as the precise determination of n_1 is uncertain in experiments (George *et al.* 2000).

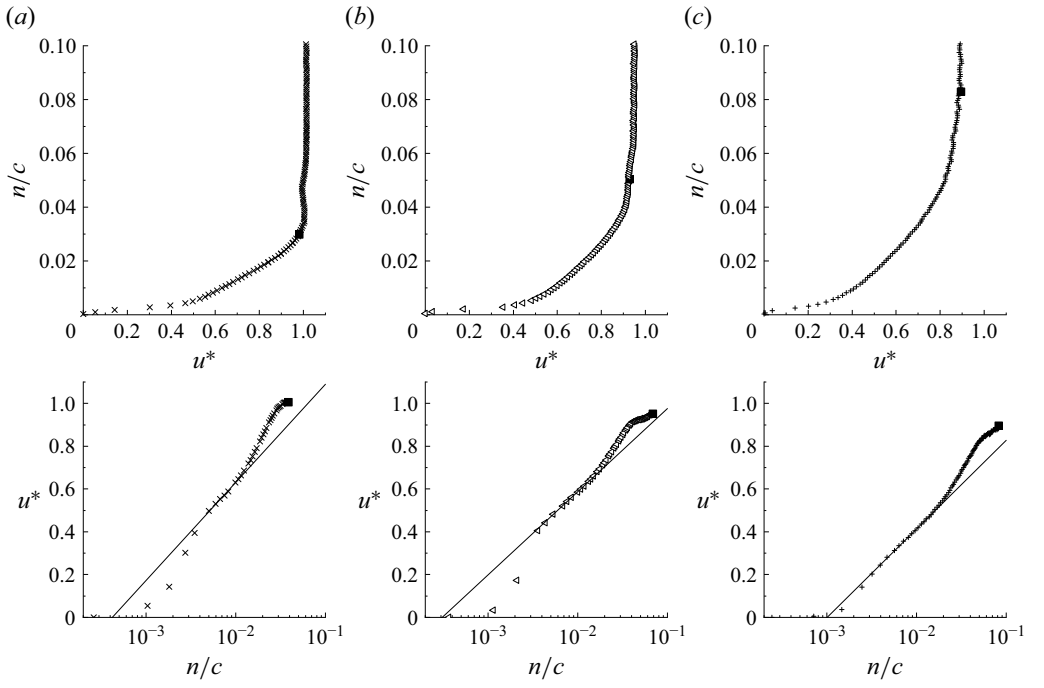

Figure 7. Sectional profiles of the dimensionless mean tangential velocity in linear and semilogarithmic scales for $\alpha = 0$ and $C_\mu = 0$ test case (baseline) at three locations: (*a*) $s/c = 0.45$ (×), (*b*) $s/c = 0.55$ (◁) and (*c*) $s/c = 0.65$ (+).

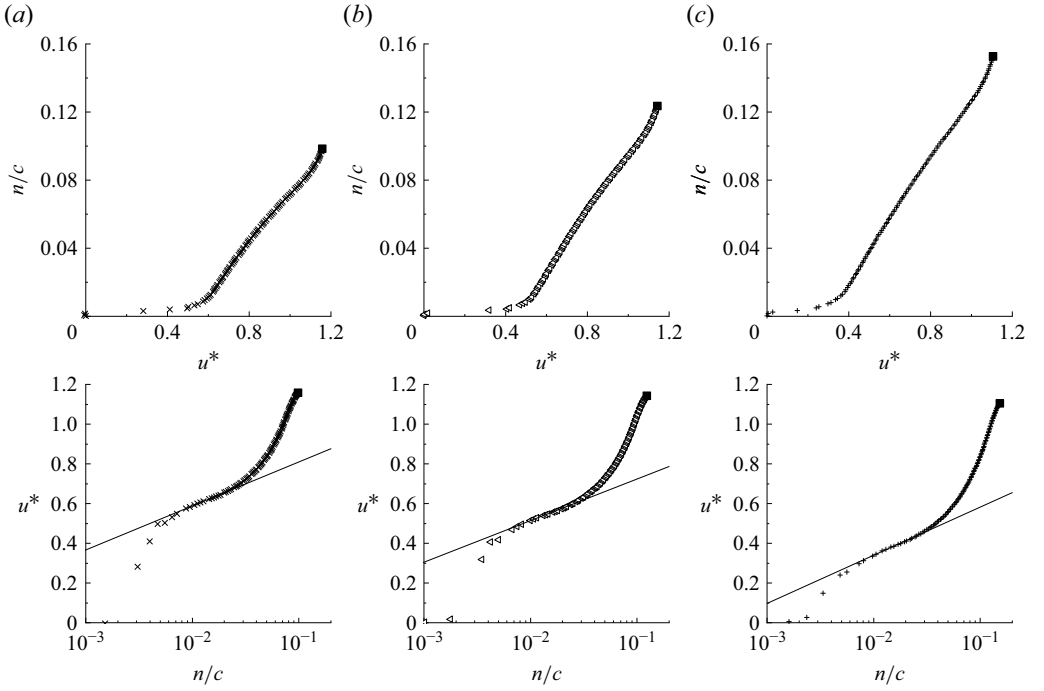

Figure 8. Sectional profiles of the dimensionless mean tangential velocity in linear and semilogarithmic scales for $\alpha = 15.0°$ and $C_\mu = 1.25 \times 10^{-3}$ test case at three locations: (*a*) $s/c = 0.40$ (×), (*b*) $s/c = 0.50$ (◁) and (*c*) $s/c = 0.60$ (+).

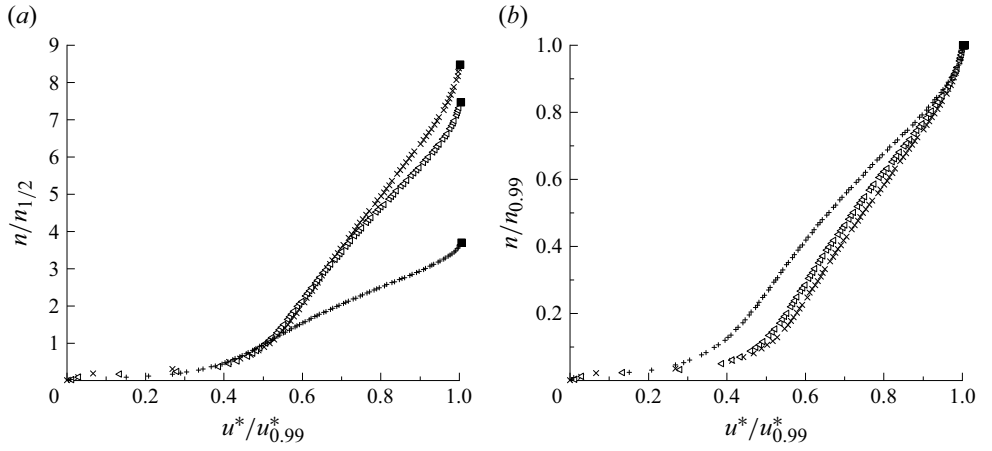

Figure 9. Scatter of the mean tangential velocity due to an improper scaling approach, collected from $\alpha = 12.5°$ and $C_\mu = 1.25 \times 10^{-3}$ test case at locations $s/c = 0.40$ (□), $s/c = 0.50$ (○) and $s/c = 0.60$ (△).

A first glance at figure 8 reveals a significant departure from classical behaviour. Although some logarithmic behaviour remains present near the wall, the remainder of the profile appears predominantly linear, a shape that is distinct from both turbulent boundary layers and wall jets. The shape of the velocity profiles suggest that the flow should be divided into three distinct shear layers, as proposed by Barenblatt, Chorin & Prostokishin (2005) for a plane turbulent wall jet. In their study, Barenblatt *et al.* (2005) scaled the inner and outer layers using power laws and noted that the data in a middle region beneath the maximum velocity location could not be collapsed onto a single curve. Following their approach, we scale the shear flow twice, first using $n_{1/2}$ and then $n_{0.99}$ as characteristic length scales, with $u_{0.99}$ as the characteristic velocity scale. The resulting scaled velocity profiles for $\alpha = 12.5°$ and $C_\mu = 1.25 \times 10^{-3}$ are presented in figure 9. While the overall pattern is similar to that observed by Barenblatt *et al.* (2005), with data scattering in the middle region, the middle region in this case is considerably wider and exhibits a pronounced linear behaviour. Following Barenblatt *et al.* (2005), we also refer to this middle layer as a mixing layer, a term that shall become more meaningful in § 3.2, § 3.3 and § 3.4.

In general, this scaling approach for turbulent wall jets, as also implied by the works of George *et al.* (2000) and Barenblatt *et al.* (2005), is effective only at high enough Reynolds numbers. The dispersion of the tangential velocity data in the middle layer is unsurprising since the Reynolds number $Re_\delta = U_\infty \delta/\nu$ was at most an order of $O(10^4)$ in these experiments. We now adopt an alternative scaling approach for the tangential velocity based on a modified form of von Kármán's defect law,

$$\widehat{U}\left(\frac{n}{n_1}\right) = \frac{u^* - u_1^*}{u_s^*}, \tag{3.2}$$

where u_s^* is the tangential characteristic velocity. Overall, with a correct choice of u_s^*, (3.2) effectively collapses the mean tangential velocity profiles onto a single curve across all test cases. The present experimental data suggests that u_s^* may not necessarily be identical to the friction velocity. For clarity, consider the scaling applied to the test case with $\alpha = 15.0°$ and $C_\mu = 0.25 \times 10^{-3}$. In this case, the tangential velocity profiles align well on a single curve when the velocity defect $u^* - u^*_{0.99}$ is scaled by $u_s^* = u^*_{0.99}$. However, when the slope of the logarithmic layer, was used for scaling, a pronounced data dispersion was observed,

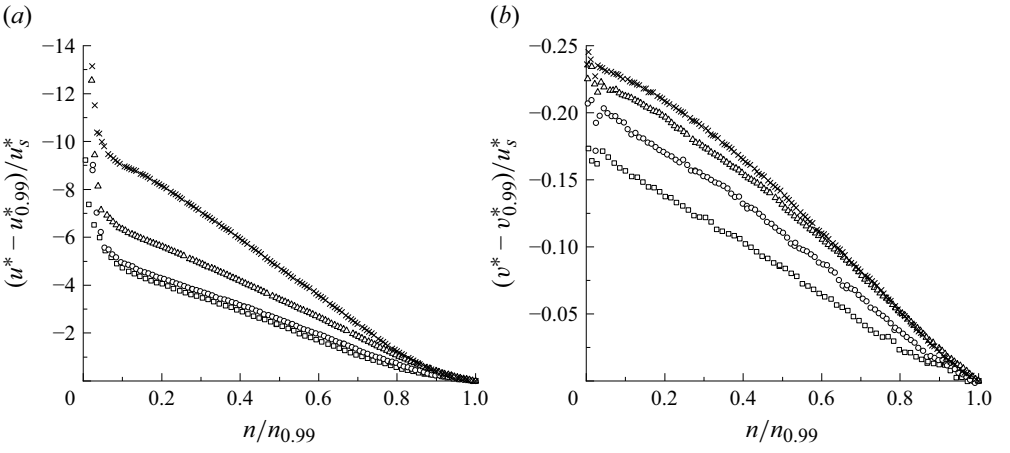

Figure 10. Scatter of the mean tangential and normal velocity defects due to improper scaling parameters, collected from $\alpha = 15.0°$ and $C_\mu = 0.25 \times 10^{-3}$ test case at locations $s/c = 0.10$ (□), $s/c = 0.20$ (○), $s/c = 0.30$ (△) and $s/c = 0.40$ (×).

as shown in figure 10(*a*). This behaviour was mostly observed for $\alpha = 12.5°$ and $\alpha = 15.0°$ cases, and not for the $\alpha = 7.5°$ test case.

Despite the success of the defect law in capturing the behaviour of the mean tangential velocity, the mean normal velocity could not be scaled using the same characteristic velocity u^*_s. Attempts to scale the mean normal velocity or its defect using u^*_s and length scale δ resulted in data scattering around one end of the profiles. An example is presented in figure 10(*b*), where the normal velocity defect $v^* - v^*_{0.99}$ is scaled by $u^*_s = u^*_{0.99}$. The scatter in the mean normal velocity upon scaling by u^*_s suggests a dissimilar scaling of the time-averaged velocity components. In other words, though the consecutive profiles could still be aligned, the appropriate scaling parameter for the normal velocity may not be the same as that for the tangential velocity. We now propose the following scaling law for the normal velocity:

$$\widehat{V}\left(\frac{n}{n_1}\right) = \frac{v^* - v^*_1}{v^*_1}. \tag{3.3}$$

For the $\alpha = 12.5°$ and $\alpha = 15.0°$ cases, only over a finite arclength along the aerofoil, scaling the data using (3.2) and (3.3) with $u^*_s = u^*_1$ led to a remarkable collapse of both velocity components onto a single curve. The results for the four test conditions at $\alpha = 12.5°$ and $\alpha = 15.0°$ are presented in figure 11. More discussion on the choice for u^*_s and similarity of the velocity components shall be presented in §§ 3.3 and 3.4.

3.2. *The formation of the mixing layer*

So far, we have established that the two velocity components in the middle layer may not scale with the same characteristic velocity. However, a physical explanation for this behaviour is still needed. This dissimilar scaling may be linked to the normal free stream velocity. To illustrate this, consider the aerofoil at two angles of attack, as shown in figure 12. From the wall's perspective, the free stream actually has two velocity components u^*_∞ and v^*_∞. For all angles of attack within $0 \leqslant \alpha \leqslant 90°$, the normal free

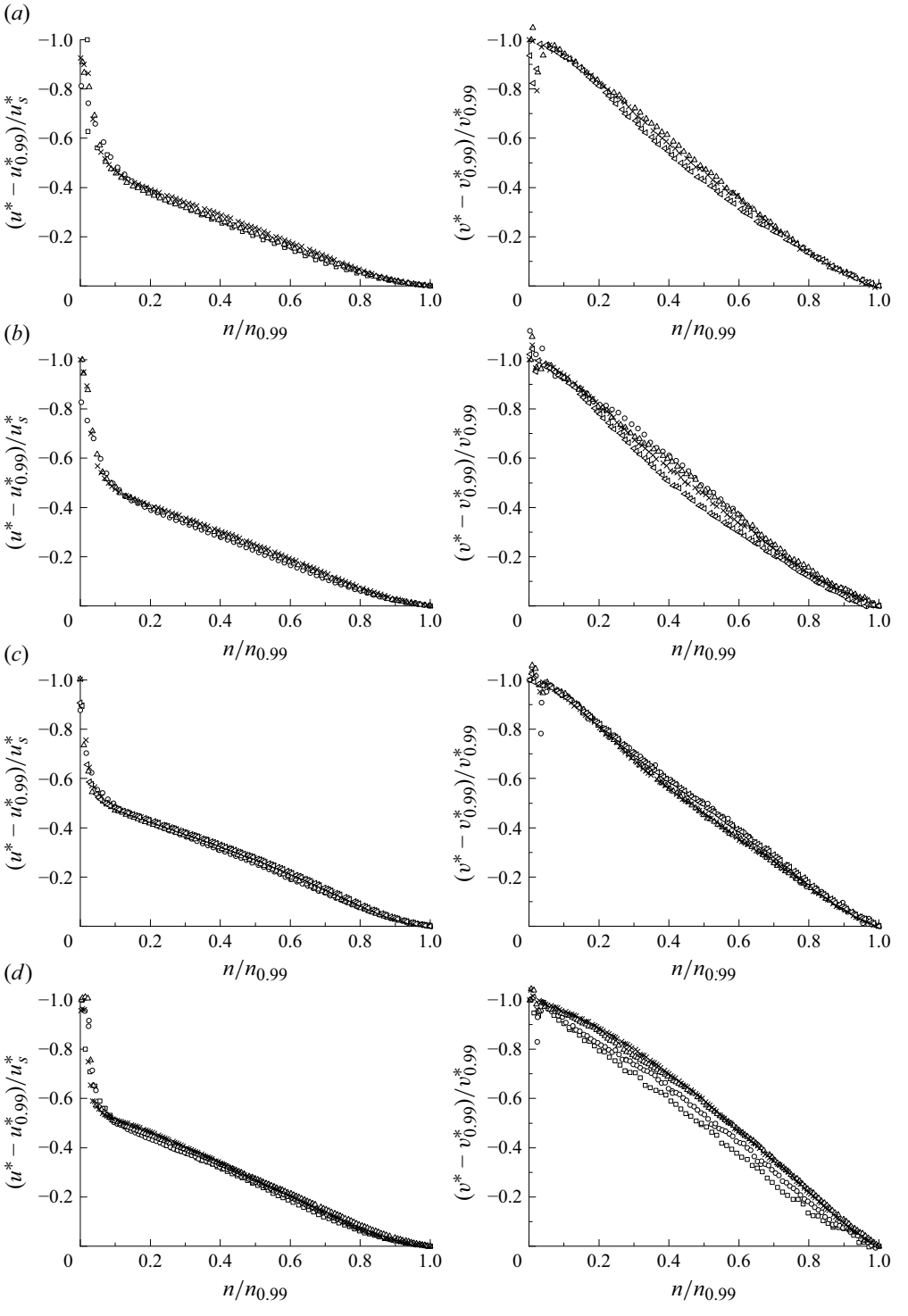

Figure 11. The dissimilar scaling of the mean velocity components at locations $s/c = 0.10$ (□), $s/c = 0.20$ (○), $s/c = 0.30$ (△), $s/c = 0.40$ (×) and $s/c = 0.50$ (◁) for four controlled cases: (*a*) $\alpha = 12.5°$ and $C_\mu = 1.25 \times 10^{-3}$, (*b*) $\alpha = 12.5°$ and $C_\mu = 0.25 \times 10^{-3}$, (*c*) $\alpha = 15.0°$ and $C_\mu = 1.25 \times 10^{-3}$, (*d*) $\alpha = 15.0°$ and $C_\mu = 0.25 \times 10^{-3}$.

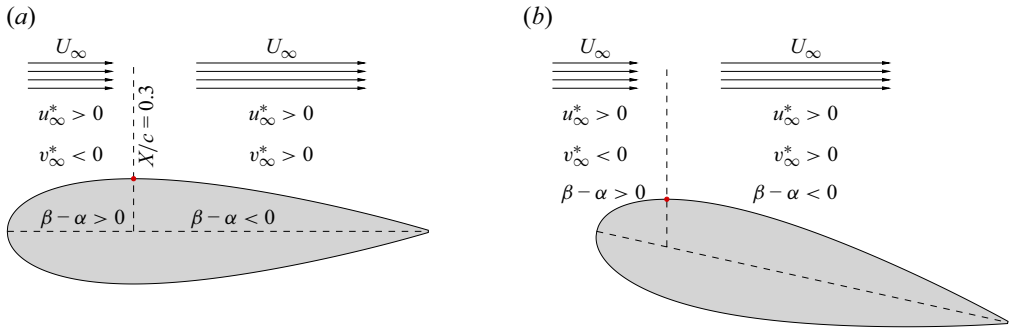

Figure 12. A schematic showing the sign of the tangential and normal free stream velocity, as observed from the wall, for two angles of attack.

stream velocity v^*_∞ switches signs from positive to negative at the zero surface-slope location. For a NACA 0025 aerofoil, this reversal occurs within $0 \leqslant X/c \leqslant 0.3$. Upstream of this point, the free stream pushes the synthetic jet towards the wall. Conversely, downstream of the reversal point, the free stream tends to pull the synthetic jet away from the wall. As the angle of attack increases, the reversal point shifts farther upstream, while the magnitude of the normal free stream velocity also increases. Hence, downstream of the reversal point, the normal velocity on the upper edge of the synthetic jet may eventually become comparable to the tangential velocity. The relative strength of the normal to tangential velocity decides the formation of the mixing layer, which depends on both the angle of attack α and the momentum coefficient C_μ.

Now, let us examine figures 13 and 14 to understand how the previous discussion relates to the present experiments. The coherent structures for various angles of attack and momentum coefficients were identified using the triple decomposition method (Hussain & Reynolds 1970), expressed by the following relation:

$$\widetilde{u_x} = \langle u_x \rangle - \overline{u_x}. \tag{3.4}$$

The synthetic jet coherent structures initially appear as pairs of counter-rotating vortices, as illustrated by the vector plots superimposed on the streamwise coherent velocity contours $\widetilde{u_x}$ in figures 13(*a*) and 13(*b*). As the flow evolves, differences between the high- and low-momentum actuation cases become evident. In the high-momentum case, the upper portion of the coherent structures penetrates the cross-flow, whereas the lower portion adheres to the wall. For the low-momentum case, on the other hand, the upper and lower portions of the coherent structures remain closer together and dissipate earlier than in the high-momentum case.

Generally, there exists a strong shear between the wall and the core of these structures, which themselves act as a significant source of cross-stream perturbations. Still, the mixing layer does not appear unless these structures are sufficiently distant from the wall since the wall significantly dampens the wall-normal velocity fluctuations. Hence, at low angles of attack and high momentum coefficients, as the normal velocity component remains relatively weak, the structures are highly organised and their core adheres to the wall. As the angle of attack increases or the momentum coefficient decreases, the free stream eventually manages to pull the coherent structures away from the wall. The substantial normal velocity fluctuations caused by the synthetic jet structures combined with the high resident shear near the wall leads to the emergence of the mixing layer, extending between the boundary layer and the central core of the jet structures. Farther downstream, these structures gradually lose momentum, becoming disorganised and

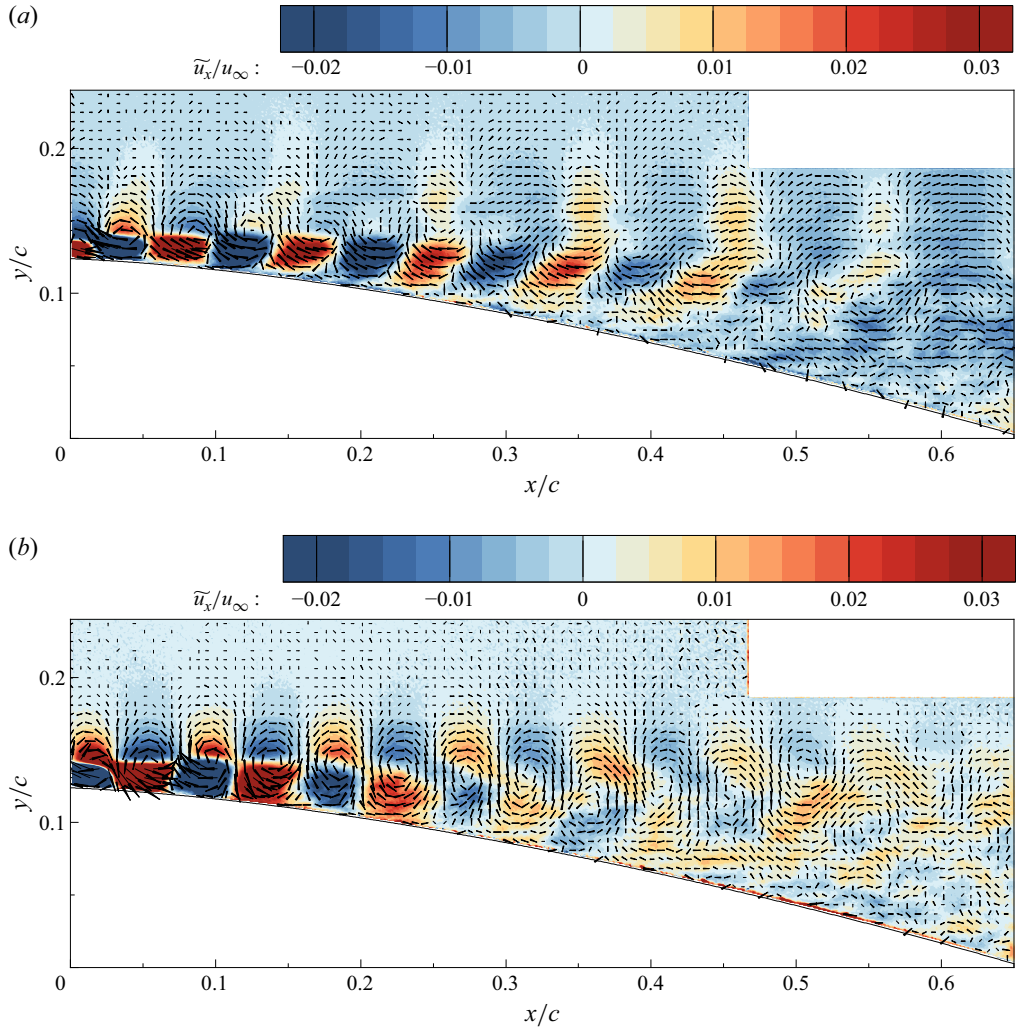

Figure 13. Contour plots of the coherent streamwise velocity at a phase angle of $\phi = 0°$ and an angle of attack of $\alpha = 12.5°$ for two momentum coefficients: (*a*) $C_\mu = 1.25 \times 10^{-3}$ and (*b*) $C_\mu = 0.25 \times 10^{-3}$.

dispersing throughout the mixing layer and jet layer before ultimately dissipating. This behaviour is particularly evident in the cases for $\alpha = 12.5°$ and $\alpha = 15.0°$, as shown in figures 14(*c*) and 14(*d*). Overall, the angle of attack and the momentum coefficient exhibit similar yet inverse effects on the development of the mixing layer. Increasing the angle of attack or decreasing the momentum coefficient enhances the normal velocity magnitude relative to the tangential velocity, pushing the onset of the mixing layer upstream and increasing its spreading rate.

3.3. *The asymptotic solution*

This section introduces an analytical solution for the mixing layer under asymptotic conditions. Let us consider a quasi-two-dimensional turbulent flow along a convex wall with a surface curvature of ϱ, where the tangential and normal velocity components are both significant. The flow has evolved over an arclength of λ from its onset at $s = s_0$, reaching a characteristic thickness of δ and a Reynolds number of $Re_\delta = U_\infty \delta/\nu$, as

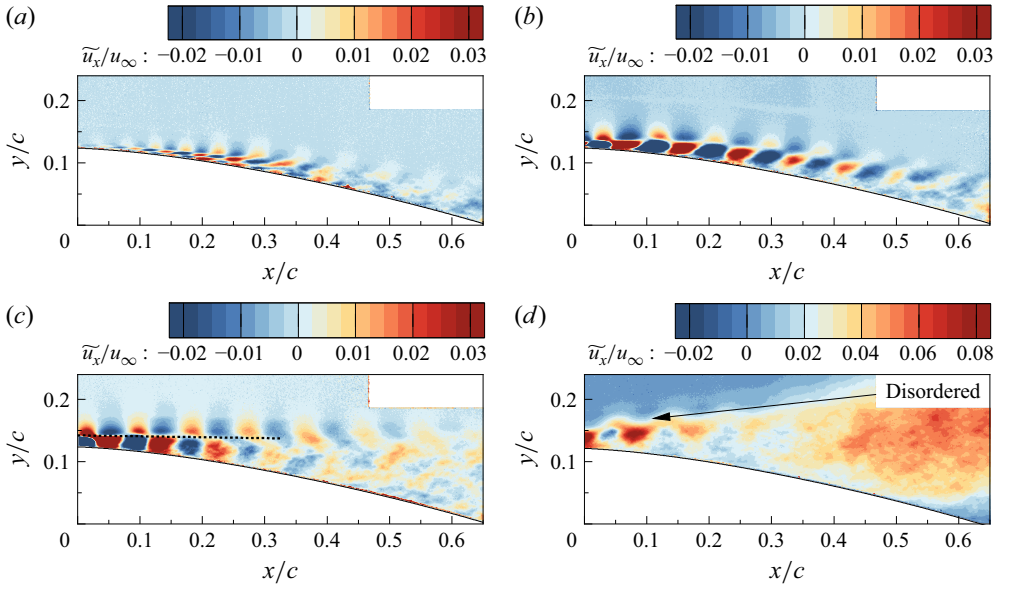

Figure 14. Contour plots of the coherent streamwise velocity at a phase angle of $\phi = 0°$ and a momentum coefficient of $C_\mu = 0.25 \times 10^{-3}$ for four angles of attack: (*a*) $\alpha = 0$, (*b*) $\alpha = 7.5°$, (*c*) $\alpha = 12.5°$ and (*d*) $\alpha = 15.0°$.

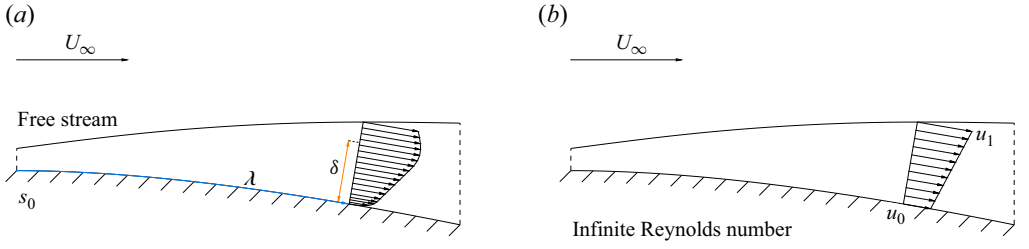

Figure 15. A schematic showing the mean tangential velocity profile at finite and infinite Reynolds numbers.

illustrated in figure 15. We seek a solution in the limit of $\delta/\lambda \ll 1$ at infinite Reynolds number, where δ/λ is the spreading rate. The curvature ratio $\varrho\delta$, which was introduced by Dean (1927) for flow inside a toroidal pipe, quantifies the ratio of centrifugal to inertial forces.

To begin the analysis, we conduct an order of magnitude examination of the velocities. The time-averaged tangential velocity has a magnitude comparable to the free stream velocity U_∞. Since the contribution of the normal velocity gradient to flow continuity may become comparable to that of the tangential velocity gradient, the order of the normal velocity can be estimated using $\partial\overline{v_n}/\partial n \sim \partial\overline{u_t}/\partial s$. The order of magnitude and the dimensionless form of the velocities and length scales are summarised as follows:

$$s - s_0 \sim O(\lambda), \qquad n \sim O(\delta), \qquad \overline{u_t} \sim O(U_\infty), \qquad \overline{v_n} \sim O\left(\frac{U_\infty \delta}{\lambda}\right), \tag{3.5}$$

$$s^* = \frac{s - s_0}{\lambda}, \qquad n^* = \frac{n}{\lambda}, \qquad u^* = \frac{\overline{u_t}}{U_\infty}, \qquad v^* = \frac{\overline{v_n}}{U_\infty}.$$

For an incompressible flow, the time-averaged continuity equation in the curvilinear coordinates (s, n) is expressed by (3.6). The dimensionless form of this equation is derived

by substituting the corresponding dimensionless variables. The result, normalised by the highest-order velocity gradient U_∞/δ, is (3.7),

$$\frac{\partial \overline{u_t}}{\partial s} + \frac{\partial (1+\varrho n)\overline{v_n}}{\partial n} = 0, \tag{3.6}$$

$$\underbrace{\frac{\delta}{\lambda}\frac{\partial u^*}{\partial s^*}}_{O(\frac{\delta}{\lambda})} + \underbrace{\frac{\delta}{\lambda}\frac{\partial v^*}{\partial n^*}}_{O(\frac{\delta}{\lambda})} + \underbrace{\varrho\delta\frac{\partial n^* v^*}{\partial n^*}}_{O\left(\varrho\delta\frac{\delta}{\lambda}\right)} = 0. \tag{3.7}$$

Our objective here is to determine the velocity profiles at infinite Reynolds number, where the viscous sublayer has vanished, and the inner, middle and outer flow regions are essentially decoupled. The boundary condition for the normal velocity at the wall remains $v^*(s^*, n^*=0)=0$ as there is no suction or blowing. Expanding the normal velocity about the wall by Taylor series, and considering the limit $\delta/\lambda \ll 1$, the series can be truncated at first order,

$$v^* = v^*(s^*,0) + n^*\frac{\partial v^*}{\partial n^*}(s^*,0) + O\left(n^{*2}\right) \xrightarrow[n^*\sim O\left(\frac{\delta}{\lambda}\right)]{\frac{\partial v^*}{\partial n^*}(s^*,0)=F(s^*)} v^* = F(s^*)n^* + O\left(\frac{\delta^2}{\lambda^2}\right). \tag{3.8}$$

The asymptotic form of the normal velocity can be determined through similarity, in contrast to plane shear flows, where the cross-stream velocity must be obtained from continuity. By defining the similarity variable $\xi = n^*/n_1^*$ and enforcing self-similarity on the normal velocity defect, we have

$$\widetilde{V}(\xi) = \frac{v^* - v_1^*}{v_1^*} = \frac{F(s^*)\left(n^* - n_1^*\right)}{F(s^*)n_1^*} \longrightarrow \widetilde{V}(\xi) = \xi - 1. \tag{3.9}$$

Hence, under the given conditions, the normal velocity must collapse onto a linear profile described by $\widetilde{V}(\xi)=\xi-1$, a trend that is already evident in figure 11. Next, by applying flow continuity and imposing self-similarity on the tangential velocity defect, we derive the asymptotic form of the tangential component,

$$\left.\begin{aligned}
&\frac{\partial u^*}{\partial s^*} + \frac{\partial (1+\varrho\lambda n^*)v^*}{\partial n^*} = 0 \longrightarrow u^* = -\int_0^{s^*} F(\varsigma)\mathrm{d}\varsigma - 2\lambda n^*\int_0^{s^*}\varrho(\varsigma)F(\varsigma)\mathrm{d}\varsigma + G(n^*),\\
&u^* - u_1^* = \left(-2\lambda\int_0^{s^*}\varrho(\varsigma)F(\varsigma)\mathrm{d}\varsigma\right)\left(n^* - n_1^*\right) + G(n^*) - G\left(n_1^*\right) \xrightarrow{G(n^*)=An^*+C}\\
&\widetilde{U}(\xi) = \frac{u^* - u_1^*}{u_s^*} = \frac{\left(A - 2\lambda\int_0^{s^*}\varrho(\varsigma)F(\varsigma)\mathrm{d}\varsigma\right)\left(n^* - n_1^*\right)}{u_s^*}\\
&u_s^* = \left(A - 2\lambda\int_0^{s^*}\varrho(\varsigma)F(\varsigma)\mathrm{d}\varsigma\right)n_1^*
\end{aligned}\right\} \longrightarrow \widetilde{U}(\xi) = \xi - 1. \tag{3.10}$$

Equation (3.10) conveys two key messages. First, when the Reynolds number reaches infinity and the spreading rate remains sufficiently low, the tangential velocity also follows the linear profile $\widetilde{U}(\xi)=\xi-1$. Second, at infinite Reynolds number, the characteristic velocity required for scaling is given by $u_s^* = (A - 2\lambda\int_0^{s^*}\varrho(\varsigma)F(\varsigma)\mathrm{d}\varsigma)n_1^*$, which

generally differs from the maximum velocity u_1^* or the friction velocity. Nonetheless, in this limit, the viscous sublayer will perish, and the tangential velocity boundary condition at the wall becomes $u_0^* = -\int_0^{s^*} F(\varsigma)\mathrm{d}\varsigma + C$. Thus, the characteristic velocity can be rewritten as $u_s^* = u_1^* - u_0^* = (A - 2\lambda \int_0^{s^*} \varrho(\varsigma)F(\varsigma)\mathrm{d}\varsigma)n_1^*$.

It can be proven that the velocities can be scaled relative to any arbitrary cross-stream location n_ε, a property reminiscent of a plane mixing layer. This scaling property can be established by following the steps outlined here

$$\left.\begin{aligned} u_\varepsilon^* = \varepsilon u_1^* + (1-\varepsilon)u_0^* \longrightarrow \frac{u_\varepsilon^* - u_1^*}{u_s^*} = \varepsilon - 1 = \widetilde{U}\left(\frac{n_\varepsilon^*}{n_1^*}\right) = \frac{n_\varepsilon^*}{n_1^*} - 1 \longrightarrow \frac{n_\varepsilon}{n_1} = \varepsilon, \\ \frac{u^* - u_\varepsilon^*}{u_s^*} = \frac{u^* - u_1^*}{u_s^*} - \frac{u_\varepsilon^* - u_1^*}{u_s^*} = \xi - \varepsilon \\ \frac{v^* - v_\varepsilon^*}{v_s^*} = \frac{v^* - v_1^*}{v_s^*} - \frac{v_\varepsilon^* - v_1^*}{v_s^*} = \xi - \varepsilon \end{aligned}\right\} \xrightarrow{\zeta = \xi - \frac{n_\varepsilon}{n_1} = \xi - \varepsilon} \begin{aligned} \widetilde{U}_\varepsilon(\zeta) = \frac{u^* - u_\varepsilon^*}{u_s^*} = \zeta \\ \widetilde{V}_\varepsilon(\zeta) = \frac{v^* - v_\varepsilon^*}{v_s^*} = \zeta \end{aligned}. \tag{3.11}$$

In the first line, it is shown that the tangential velocity achieves a value of u_ε at the cross-stream position $n_\varepsilon/n_1 = \varepsilon$. The subsequent steps reveal that the velocity deficits, when scaled about $\xi = \varepsilon$ by u_s^* and v_s^*, assume the forms $\widetilde{U}_\varepsilon(\zeta) = \zeta$ and $\widetilde{V}_\varepsilon(\zeta) = \zeta$, where $-\varepsilon \leqslant \zeta \leqslant 1 - \varepsilon$. The asymptotic solution of the velocity is summarised as follows:

$$v^* = F(s^*)n^*, \tag{3.12}$$

$$u^* = -\int_0^{s^*} F(\varsigma)\mathrm{d}\varsigma + \left(A - 2\lambda \int_0^{s^*} \varrho(\varsigma)F(\varsigma)\mathrm{d}\varsigma\right) n^* + C. \tag{3.13}$$

3.4. *The incomplete similarity*

In § 3.3, we derived an asymptotic solution for the flow at infinite Reynolds number. In this limit, the flow behaves as an equilibrium mixing layer, both velocities scale with their respective velocity differences, and the shape of the velocity profile remains unchanged across all locations. At finite Reynolds numbers, however, two overlap regions appear at the edges of the middle layer. In this case, the flow is no longer purely a mixing layer or a boundary layer, but instead exhibits characteristics of both. Since the 1930s, two principal models have been proposed to describe the overlap regions: the logarithmic law (von Kármán 1930) and the power law (Barenblatt 1993). Although both are derived with comparable rigour, the logarithmic law relies on the assumption that molecular viscosity is negligible. In this context, the logarithmic and power laws are expressed as follows:

$$\widetilde{L}(\xi) = \ln(\xi), \tag{3.14}$$

$$\widetilde{L}(\xi) = \xi^\epsilon - 1. \tag{3.15}$$

The extent to which the flow resembles either a boundary layer or a mixing layer strongly depends on the local Reynolds number Re_δ. To initiate our analysis, we examine a relatively low Reynolds number case with $\alpha = 7.5°$ and $C_\mu = 0.25 \times 10^{-3}$. Our results show that at these lower Reynolds numbers, especially during the early stages of mixing layer development, both overlap regions conform to the logarithmic law. This behaviour is illustrated in the scaled velocity profiles shown at four representative locations in figure 16. Notably, at $s/c = 0.1$, the velocity profile can be entirely described by the logarithmic law. As the local Reynolds number increases, a transition occurs, and the mixing layer emerges

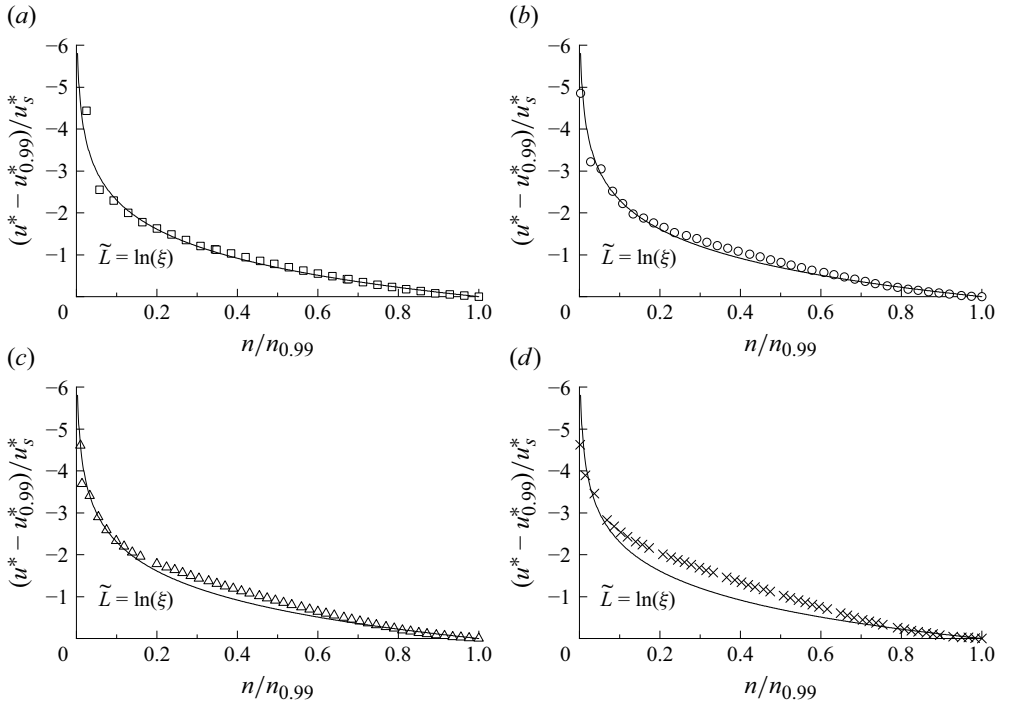

Figure 16. Evolution of the mixing layer for $\alpha = 7.5°$ and $C_\mu = 0.25 \times 10^{-3}$ test case compared with the logarithmic law (solid line) at four locations: (*a*) $s/c = 0.10$ (□), (*b*) $s/c = 0.20$ (○), (*c*) $s/c = 0.30$ (△) and (*d*) $s/c = 0.40$ (×).

at some streamwise location. However, since the characteristic velocity remains close to the friction velocity, the logarithmic law continues to provide a reasonable description of both overlap regions. The profile shape gradually evolves with increasing local Reynolds number, incorporating a linear segment associated with the mixing layer. Consequently, the tangential velocity profile remains Reynolds-number-dependent, and its similarity is incomplete.

At high Reynolds numbers, such as in cases with $\alpha = 12.5°$ and $15.0°$, the scaling becomes largely insensitive to variations in the local Reynolds number as these cases are relatively close to the equilibrium mixing layer. In these cases, the characteristic velocity required to align successive profiles closely approximates the mixing layer velocity difference $u_1^* - u_0^*$. However, the inner overlap region lies much closer to the wall, where the molecular viscosity can no longer be neglected. As a result, the power law is required to achieve consistent scaling across both overlap regions. Unlike the low Reynolds number regime, where the overlap region shape remains fixed, the shape in this high Reynolds number regime varies with the Reynolds number, due to the Reynolds number dependence of the power-law exponent. Figure 17 shows the velocity profiles at four selected locations for the case with $\alpha = 15.0°$ and $C_\mu = 1.25 \times 10^{-3}$. The profiles are overlaid with both power law fits and the asymptotic mixing layer line, highlighting the increasing linearity of the profiles and the proximity of the flow to the equilibrium mixing layer.

The preceding discussions, particularly figures 16 and 17, demonstrate that, regardless of the specific law used to describe the overlap regions, the entire velocity profile may be interpreted as a boundary layer influenced by contributions from the mixing layer. Following Coles (1956), we propose an analogue of the law of the wake to represent the

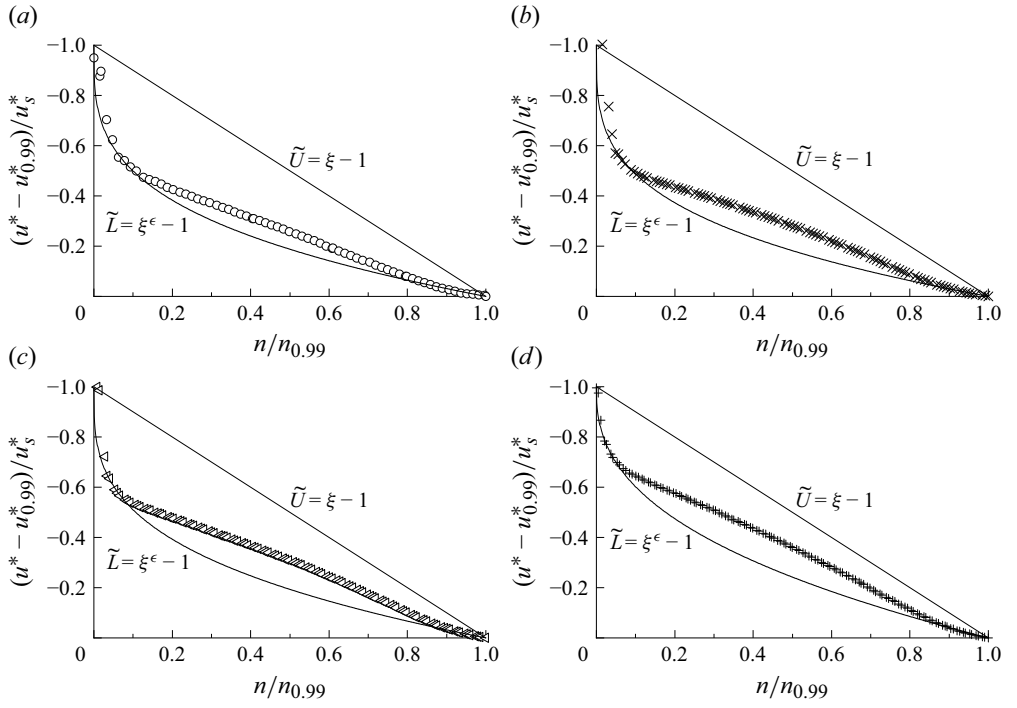

Figure 17. Evolution of the mixing layer for $\alpha = 15.0°$ and $C_\mu = 1.25 \times 10^{-3}$ test case compared with the power law (solid line) at four locations: (*a*) $s/c = 0.20$ (○), (*b*) $s/c = 0.40$ (×), (*c*) $s/c = 0.50$ (◁) and (*d*) $s/c = 0.60$ (+).

effect of the mixing layer embedded within a turbulent boundary layer,

$$\widehat{U}(\xi) = \widetilde{L}(\xi) - \Pi \widehat{M}(\xi). \tag{3.16}$$

By analogy with Coles' law of the wake, we refer to the parameter Π in (3.16) as the mixing strength. Using the current experimental data, we aim to investigate the shape of the mixing function $\widehat{M}(\xi)$ for finite values of Π. The most direct approach to determining the shape of the mixing function is to subtract the equilibrium mixing layer profile from a boundary layer profile that is infinitesimally close to it. Mathematically, this limiting state corresponds to the power-law exponent ϵ approaching unity. In this asymptotic state, the mixing function $\widehat{M}(\xi)$ takes the following form:

$$\widetilde{\Pi} = \max\left(\widetilde{L}(\xi) - \widetilde{U}(\xi)\right) = \epsilon^{\frac{\epsilon}{(1-\epsilon)}} - \epsilon^{\frac{1}{(1-\epsilon)}}, \tag{3.17}$$

$$\widetilde{M}(\xi) = \lim_{\epsilon \to 1} \frac{\widetilde{L}(\xi) - \widetilde{U}(\xi)}{\widetilde{\Pi}} = \lim_{\epsilon \to 1} \frac{\xi^\epsilon - \xi}{\widetilde{\Pi}} = -\xi \ln(\xi). \tag{3.18}$$

The asymptotic shape of the mixing function, along with the variation of mixing strength as $\epsilon \to 1$, is illustrated in figure 18. Evidently, while the mixing strength approaches zero in this limit, the mixing function itself converges to a well-defined shape. Specifically, it tends towards $\widetilde{M}(\xi) = -\xi \ln(\xi)$, as shown in figure 18(*a*).

If the mixing function remains self-similar, we would expect the shape observed in figure 18(*a*) to be preserved, regardless of the law used to describe the base boundary layer. To investigate this, we examine the contribution of the mixing layer for both cases presented earlier in figures 16 and 17. The results, obtained by subtracting either the logarithmic law or the power law from the velocity profiles, are shown in figures 19 and 20,

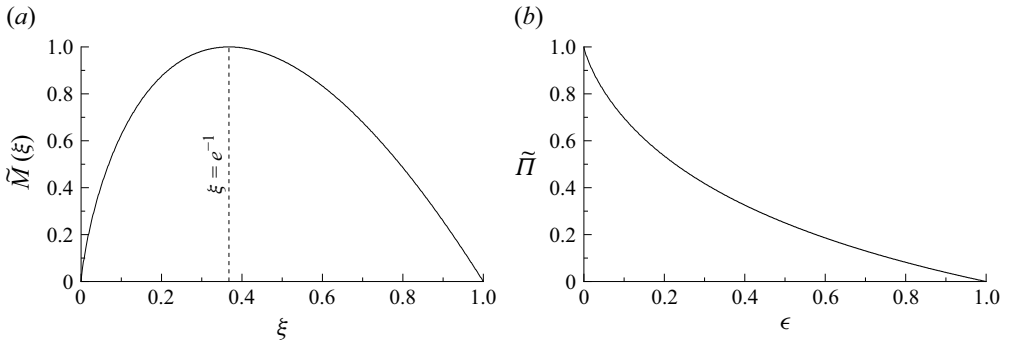

Figure 18. The asymptotic shape of the mixing function and the variations of the mixing strength with respect to the power-law exponent.

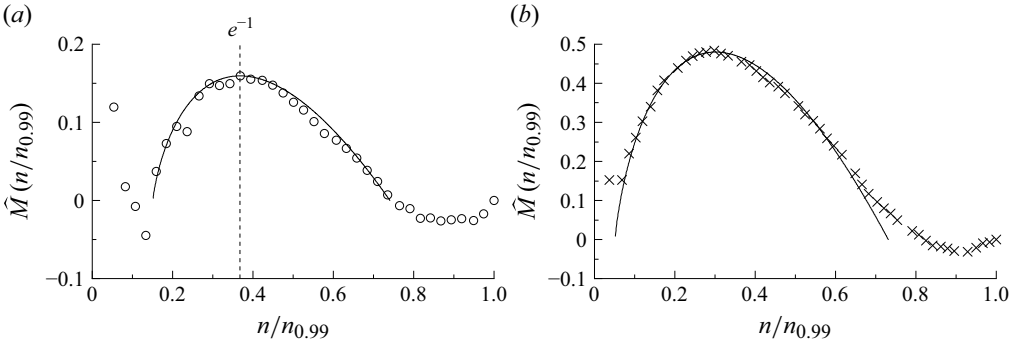

Figure 19. Distribution of the mixing function for $\alpha = 7.5°$ and $C_\mu = 0.25 \times 10^{-3}$ test case compared with the asymptotic shape (solid line) at two locations: (*a*) $s/c = 0.20$ (∘) and (*b*) $s/c = 0.40$ (×).

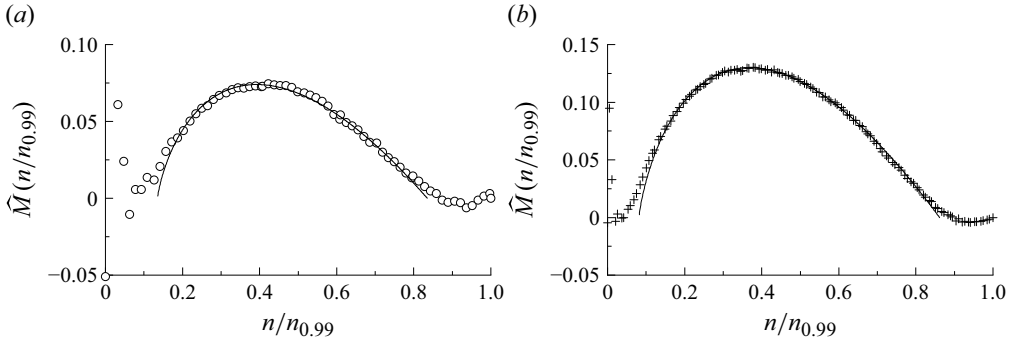

Figure 20. Distribution of the mixing function for $\alpha = 15.0°$ and $C_\mu = 0.25 \times 10^{-3}$ test case compared with the asymptotic shape (solid line) at two locations: (*a*) $s/c = 0.20$ (∘) and (*b*) $s/c = 0.60$ (+).

respectively. These figures confirm our earlier hypothesis. Irrespective of the boundary layer description, the subtraction yields the same shape observed in figure 18(*a*). A notable feature of the mixing function is its asymmetry, which distinguishes it from the wake function observed by Coles (1956). Consequently, the sine-squared function, commonly employed to represent the wake function, is not well-suited for describing the mixing function. Overall, using any smooth empirical function $\widetilde{Q}(\xi)$ that accurately captures the

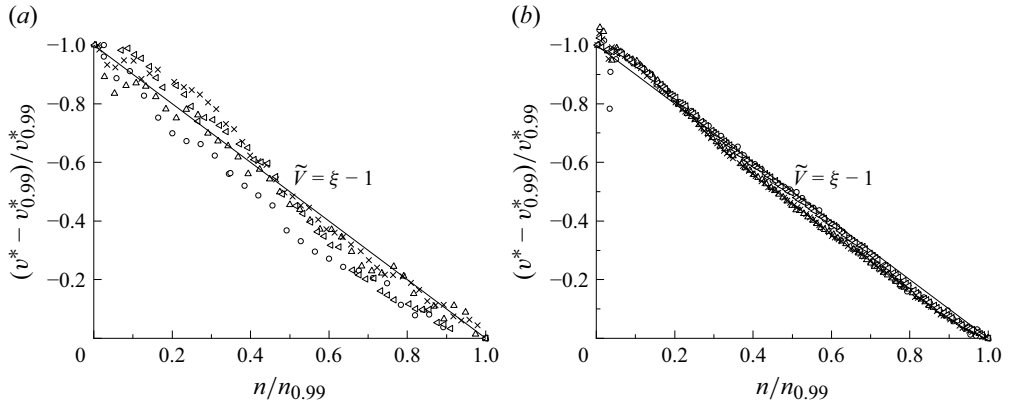

Figure 21. Distribution of the scaled normal velocity compared with the asymptotic shape (solid line) at locations $s/c = 0.20$ (○), $s/c = 0.30$ (△), $s/c = 0.40$ (×) and $s/c = 0.50$ (◁) for two test cases: (*a*) $\alpha = 7.5°$ and $C_\mu = 0.25 \times 10^{-3}$ and (*b*) $\alpha = 15.0°$ and $C_\mu = 1.25 \times 10^{-3}$.

shape shown in figure 18(*a*), we can express the tangential velocity profile as follows:

$$\widehat{U}(\xi) = \widetilde{L}(\xi) - \Pi\,\widetilde{Q}(\xi). \tag{3.19}$$

We conclude this section by comparing the distribution of the normal velocity with its asymptotic shape, as shown in figure 21. In contrast to the tangential velocity, the normal velocity can be consistently scaled using the velocity difference v_1^*, with the data closely following the asymptotic line across the range of Reynolds numbers tested. A more detailed discussion of the normal velocity is deferred to § 3.5.

3.5. *Curvature effects*

In this section, we examine whether the surface curvature influences the velocity gradients $\partial v^*/\partial n^*$ and $\partial u^*/\partial n^*$, focusing on regions with high local Reynolds numbers where the flow behaves more like a mixing layer. The effect of surface curvature on the normal velocity is inherently complex. As discussed in § 3.2, the normal free stream velocity, which drives the gradient $\partial v^*/\partial n^*$, is non-zero and, according to (2.2), depends on both the angle of attack and the local slope of the aerofoil, with $v^*_\infty = \sin(\alpha - \beta)$. As a result, it is not possible to decouple the curvature effects from those of the pressure gradient. Therefore, our interest here lies in understanding the combined influence of these effects on the normal velocity gradient $\partial v^*/\partial n^*$. The experimental data indicate that, for cases with lower angles of attack and higher momentum coefficients, specifically up to $\alpha = 12.5°$ and $C_\mu = 1.25 \times 10^{-3}$, the slope of the normal velocity gradient remains largely unchanged. In contrast, for the remaining cases where the combined effect of curvature and pressure gradient is more pronounced, the gradient slope gradually decreases along the aerofoil. For illustration, two representative cases are compared in figure 22.

To further investigate this behaviour, we expand the slope of the normal velocity gradient in the asymptotic solution $F(s^*)$ about the onset of the mixing layer using the Taylor series,

$$F(s^*) = F(0) + \frac{\mathrm{d}F}{\mathrm{d}s^*}(0)s^* + \frac{1}{2}\frac{\mathrm{d}^2F}{\mathrm{d}s^{*2}}(0)s^{*2} + O\big(s^{*3}\big). \tag{3.20}$$

In general, near the onset, $F(s^*)$ can be approximated by its zeroth-order term. Experimental observations show that when the mixing layer is allowed to develop naturally, which is under minimal combined effects of pressure gradient and surface

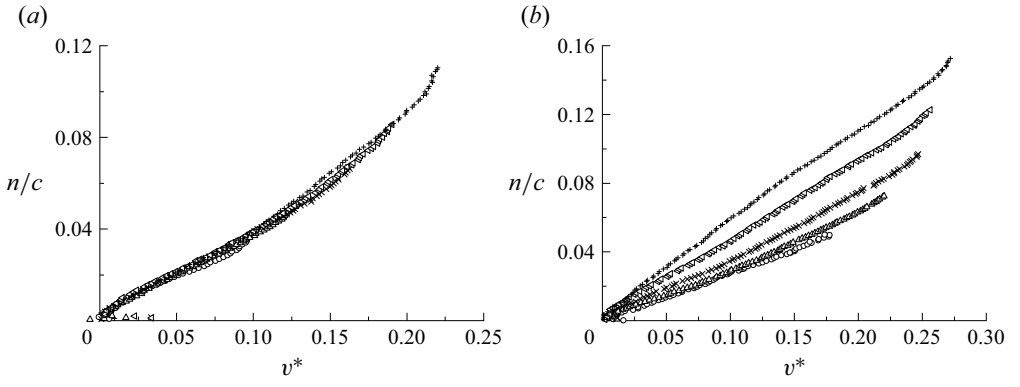

Figure 22. The s-contours of the dimensionless mean normal velocity at locations $s/c = 0.20$ (○), $s/c = 0.30$ (△), $s/c = 0.40$ (×), $s/c = 0.50$ (◁) and $s/c = 0.60$ (+) for two test cases: (*a*) $\alpha = 12.5°$ and $C_\mu = 1.25 \times 10^{-3}$ and (*b*) $\alpha = 15.0°$ and $C_\mu = 1.25 \times 10^{-3}$.

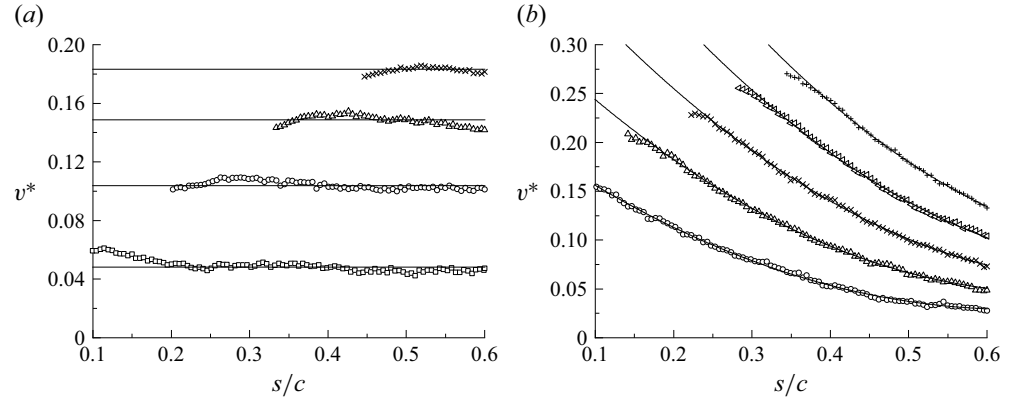

Figure 23. The n-contours of the dimensionless mean normal velocity at locations $n/c = 0.02$ (□), $n/c = 0.04$ (○), $n/c = 0.06$ (△), $n/c = 0.08$ (×), $n/c = 0.10$ (◁) and $n/c = 0.12$ (+) for two test cases: (*a*) $\alpha = 12.5°$ and $C_\mu = 1.25 \times 10^{-3}$ and (*b*) $\alpha = 15.0°$ and $C_\mu = 0.25 \times 10^{-3}$.

curvature, the function $F(s^*)$ remains approximately constant over the full development length. This implies that the normal velocity gradient $\partial v^*/\partial n^*$ is preserved. Such behaviour was observed in three previously discussed cases, that is both $\alpha = 7.5°$ configurations, as well as the $\alpha = 12.5°$ and $C_\mu = 1.25 \times 10^{-3}$ case. In contrast, when the combined influence of surface curvature and pressure gradient increases, $F(s^*)$ can no longer be truncated at the zeroth order and begins to exhibit higher-order behaviour. For example, in the $\alpha = 12.5°$ and $C_\mu = 0.25 \times 10^{-3}$ and $\alpha = 15.0°$ and $C_\mu = 1.25 \times 10^{-3}$ cases, the function $F(s^*)$ exhibits a linear decrease. In the most extreme case, that is $\alpha = 15.0°$ and $C_\mu = 0.25 \times 10^{-3}$ with the highest angle of attack and the lowest momentum coefficient, even a first-order approximation proved insufficient, and $F(s^*)$ exhibited a parabolic decay. The n-contours of the dimensionless mean normal velocity for two representative cases are shown in figures 22 and 23, illustrating both the invariance of the normal velocity profile and the parabolic decay observed under strong curvature and pressure gradient conditions. Figure 23 highlights the need for higher-order Taylor series truncations at increased angles of attack and reduced momentum coefficients.

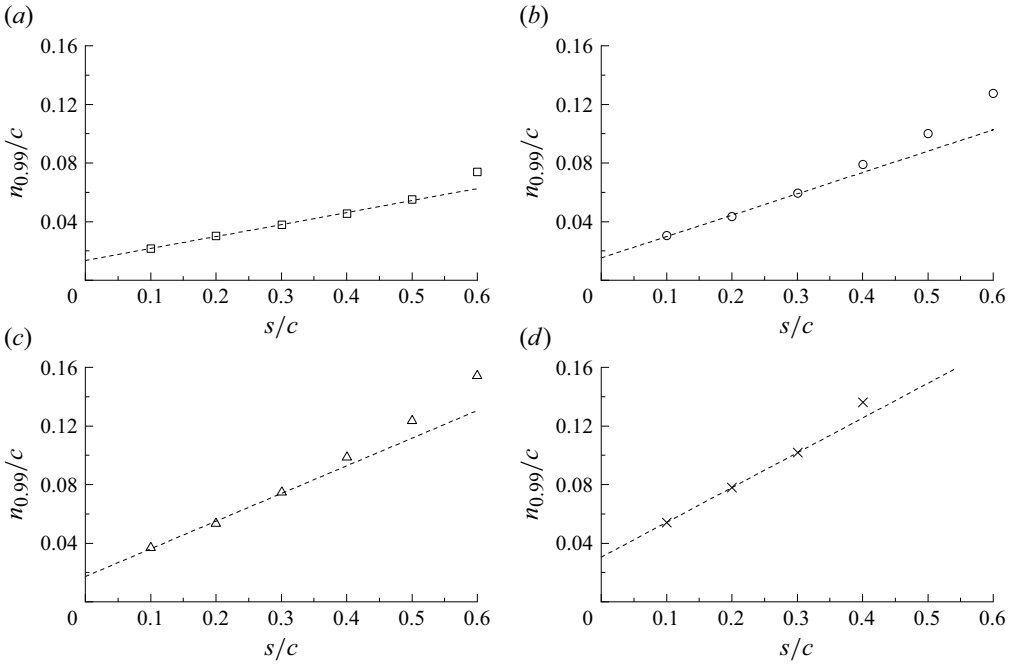

Figure 24. The spreading of the boundary layer for four test conditions: (*a*) $\alpha = 7.5°$ and $C_\mu = 0.25 \times 10^{-3}$ (□), (*b*) $\alpha = 12.5°$ and $C_\mu = 0.25 \times 10^{-3}$ (○), (*c*) $\alpha = 15.0°$ and $C_\mu = 1.25 \times 10^{-3}$ (△), (*d*) $\alpha = 15.0°$ and $C_\mu = 0.25 \times 10^{-3}$ (×).

A similar argument can be made for the spreading rate. It is well known that the spreading rate of turbulent wall jets is nonlinear and smaller than that of free jets. While the exact comparison between the spreading rate of this flow and a turbulent wall jet for a given momentum input remains unclear, the flow appears to spread at the very least linearly, when it is not disturbed. The spreading rate generally becomes nonlinear as the angle of attack increases or the momentum coefficient decreases, as shown in figure 24. The maximum spreading rate for the extreme case with $\alpha = 15.0°$ and $C_\mu = 0.25 \times 10^{-3}$ was around 25 %.

Unlike the normal velocity, surface curvature directly affects the tangential velocity gradient $\partial u^*/\partial n^*$. The s-contours of the dimensionless mean tangential velocity for two test cases are shown in figure 25. According to the asymptotic solution, the tangential velocity gradient is given by $\partial u^*/\partial n^* = A - 2\lambda \int_0^{s^*} \varrho(\varsigma) F(\varsigma) \mathrm{d}\varsigma$, indicating a clear dependence on curvature, even under conditions where the flow evolves naturally and $F(s^*) = F(0) = B$. To isolate the effect of curvature, we consider two cases in which the normal velocity remains nearly constant along the streamwise direction, as shown in figure 25. In fact, looking at figure 26, we observe that the slope of the profiles changes more rapidly upstream, where the curvature magnitude is larger. Eventually, as the curvature diminishes closer to the trailing edge, the slope gradually stabilises and approaches a constant value.

Next, we examine the rotation of the fluid elements around the wall using the mean spanwise vorticity for the cases where $F(s^*) = F(0) = B$. The time-averaged vorticity equation in curvilinear coordinates (s, n) is stated by (3.21). The dimensionless form of this equation, normalised by the highest-order velocity gradient U_∞/δ, is presented in (3.22) below,

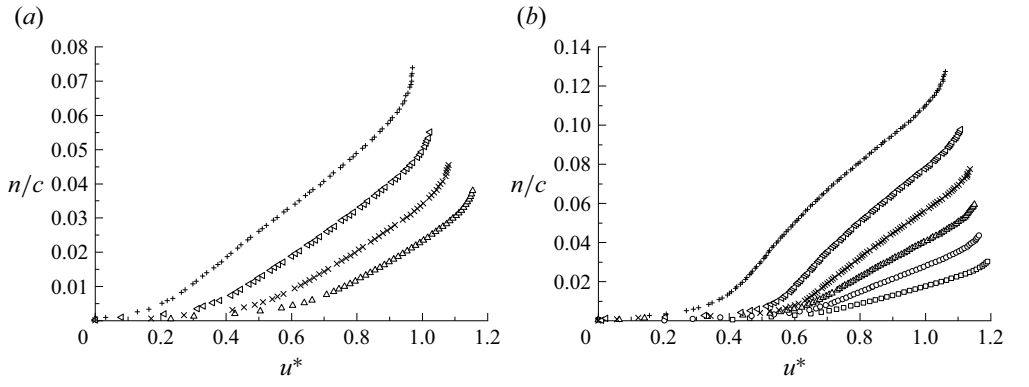

Figure 25. The s-contours of the dimensionless mean tangential velocity at locations $s/c = 0.10$ (□), $s/c = 0.20$ (○), $s/c = 0.30$ (△), $s/c = 0.40$ (×), $s/c = 0.50$ (◁) and $s/c = 0.60$ (+) for two test cases: (*a*) $\alpha = 7.5°$ and $C_\mu = 0.25 \times 10^{-3}$ (□) and (*b*) $\alpha = 12.5°$ and $C_\mu = 1.25 \times 10^{-3}$ (○).

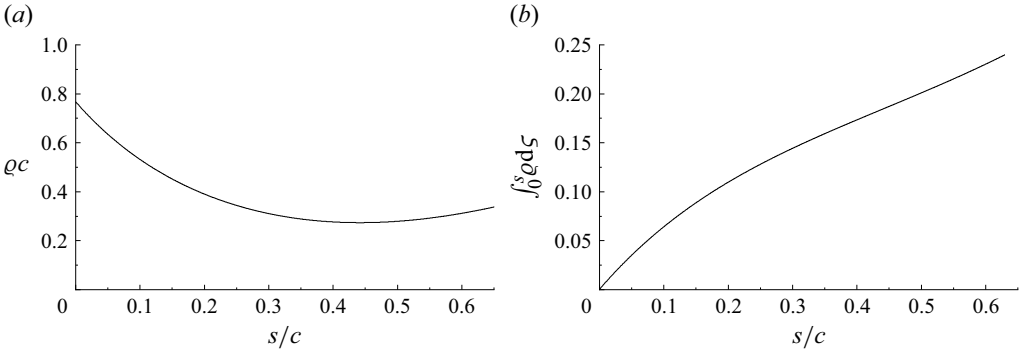

Figure 26. Distribution of the curvature parameters with respect to the arclength for a NACA 0025 aerofoil.

$$\frac{\partial \overline{v_n}}{\partial s} - \frac{\partial (1+\varrho n)\overline{u_t}}{\partial n} = (1+\varrho n)\overline{\Omega_z}, \tag{3.21}$$

$$\underbrace{\frac{\delta}{\lambda}\frac{\partial u^*}{\partial n^*}}_{O(1)} + \underbrace{\varrho\delta\frac{\partial n^* u^*}{\partial n^*}}_{O(\varrho\delta)} - \underbrace{\frac{\delta}{\lambda}\frac{\partial v^*}{\partial s^*}}_{O\left(\frac{\delta^2}{\lambda^2}\right)} = -(1+\varrho\lambda n^*)\frac{\overline{\Omega_z}\delta}{U_\infty}. \tag{3.22}$$

Under the conditions $\delta/\lambda \ll 1$, $\varrho\delta \ll 1$ and $F(s^*) = B$, the time-averaged vorticity can be determined by neglecting terms of order δ^2/λ^2 and $\varrho^2\delta^2$ and substituting the asymptotic velocity expressions into (3.22),

$$\left.\begin{aligned} u^* &= \left(A - 2B\lambda\int_0^{s^*}\varrho(\varsigma)\mathrm{d}\varsigma\right)n^* - Bs^* + C \\ v^* &= Bn^* \end{aligned}\right\} \xrightarrow{\frac{1}{1+\varrho\lambda n^*} = 1-\varrho\lambda n^* + O(\varrho^2\delta^2)}$$

$$\frac{\overline{\Omega_z}\lambda}{U_\infty} = \varrho\lambda(Bs^* - C)(1-\varrho\lambda n^*) + \left(2B\lambda\int_0^{s^*}\varrho(\varsigma)\mathrm{d}\varsigma - A\right)(1+\varrho\lambda n^*). \tag{3.23}$$

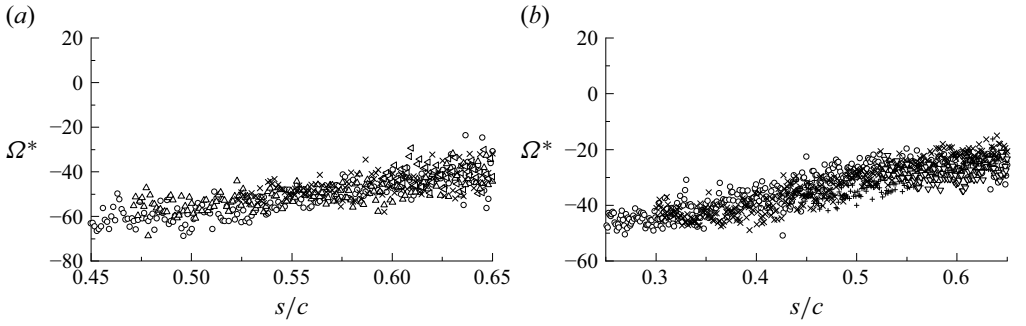

Figure 27. The n-contours of the dimensionless mean spanwise vorticity at locations $n/c = 0.02$ (○), $n/c = 0.03$ (△), $n/c = 0.04$ (×), $n/c = 0.05$ (◁), $n/c = 0.06$ (+) and $n/c = 0.08$ (△), demonstrating the clockwise rotation of fluid elements inside the mixing layer for two test cases: (*a*) $\alpha = 7.5°$ and $C_\mu = 0.25 \times 10^{-3}$ and (*b*) $\alpha = 12.5°$ and $C_\mu = 1.25 \times 10^{-3}$.

In the limit of $\varrho\lambda \ll 1$, another simplification can be applied to the vorticity distribution given in (3.23). Under this condition, the variations in the radius of curvature across the entire length of the mixing layer λ become negligible. Consequently, we expect $\int_0^{s^*} \varrho(\varsigma)\mathrm{d}\varsigma \approx \varrho s^*$.

The conditions $\varrho\delta \ll 1$ and $\varrho\lambda \ll 1$ are well satisfied over the second-half of the aerofoil ($s/c > 0.15$), as shown in figure 26. Note that for the highest Reynolds number cases, $\delta/c \sim O(10^{-1})$, and therefore $\varrho\delta \sim O(10^{-2})$ within $s/c > 0.15$. With these considerations, (3.23) simplifies to

$$\Omega^* = \frac{\overline{\Omega_z}}{\varrho U_\infty} = (Bs^* - C)(1 - \varrho\lambda n^*) + \left(2Bs^* - \frac{A}{\varrho\lambda}\right)(1 + \varrho\lambda n^*). \tag{3.24}$$

Equation (3.24) carries significant implications regarding the effects of curvature on the mixing layer. First, as $\varrho\delta \to 0$, the vorticity behaves as $\Omega^* = 3Bs - C - Ar_0/\lambda$, suggesting that Ω^* is expected to increase linearly along the surface. Second, fluid elements rotate along the wall with a vorticity magnitude $\overline{\Omega_z} = \varrho U_\infty \Omega^*$, which is proportional to the local surface curvature ϱ. As a result, the mixing layer tends to adhere to the wall, with this adherence gradually weakening as the mixing layer develops along the surface due to the positive normal velocity gradient $F(0) = B$. The asymptotic behaviour of the vorticity is evident from the n-contour plots of the dimensionless vorticity for the two test cases shown in figure 27. The tendency of the mixing layer to adhere to the wall is also apparent in the contour plots presented earlier in figures 13(*a*) and 14(*b*).

4. Summary and conclusion

The development of the turbulent boundary layer over a NACA 0025 aerofoil at a constant reduced frequency was investigated experimentally across four angles of attack and two distinct momentum coefficients. The measured velocity field was decomposed into normal and tangential components. By applying various scaling approaches from turbulent boundary layer and wall jet literature, it was observed that the resulting boundary layer differs notably from both canonical boundary layers and wall jets. In particular, a region between the wall and the point of maximum velocity exhibited a distinct linear trend. Following the terminology of Barenblatt *et al.* (2005), this region was referred to as a mixing layer.

The theory developed by George *et al.* (2000) for turbulent wall jets highlighted that the characteristic velocity scale needed to collapse the Reynolds stresses may differ from that required for scaling the mean velocities. The present study showed that such dissimilarity in scaling is not limited to Reynolds stresses. Specifically, while each velocity defect could be locally scaled over a limited extent, the characteristic velocity needed for collapse varied between the normal and tangential components. This dissimilarity was attributed to the prominence of the normal free stream velocity, which becomes more significant as the angle of attack increases or the momentum coefficient decreases. A basic physical explanation was proposed, linking the formation of the mixing layer to the magnitude of the normal free stream velocity and the distance of the jet structures from the wall.

An asymptotic solution was introduced to describe the flow behaviour at infinite Reynolds number, where the flow approaches an equilibrium mixing layer. Unlike conventional turbulent boundary layers and turbulent wall jets, where the normal velocity goes to zero, the asymptotic solution predicted a linear distribution of the normal velocity. At the finite Reynolds numbers examined in this study, two overlap regions emerged above and below the central layer, and the flow exhibited a hybrid character, combining features of both boundary layers and mixing layers. At relatively low local Reynolds numbers, the overlap regions followed the logarithmic law and the flow behaviour more closely resembled that of a turbulent boundary layer. As the Reynolds number increased, the overlap regions were better captured by Reynolds-number-dependent power laws, and the flow transitioned towards mixing layer behaviour, with the velocity difference serving as the appropriate characteristic scale.

The similarity of the tangential velocity was incomplete, as the shape of the velocity profiles evolved with the local Reynolds number along the aerofoil. Regardless of whether the logarithmic or power law was used to describe the overlap regions, the overall profiles could be interpreted as a base boundary layer with an added contribution from the mixing layer, reminiscent of Coles' law of the wake. However, the residual function observed here was asymmetric and differed from that of conventional turbulent boundary layers. An analytical expression for the mixing function was derived from the asymptotic analysis, and notably, its shape remained invariant across the range of Reynolds numbers considered.

The effects of curvature were investigated for both the tangential and normal velocity components. For the normal velocity, curvature and pressure gradient effects could not be independently isolated. However, their combined influence was found to be minimal at lower angles of attack and higher momentum coefficients, where the normal velocity gradient remained nearly constant along the development length. At higher angles of attack and lower momentum coefficients, the normal velocity exhibited a linear or parabolic decay, which was explained by the Taylor series expansion of the normal velocity gradient about the onset of the mixing layer. In contrast, curvature had a direct and measurable impact on the tangential velocity gradient, leading to a gradual decrease in its magnitude. Vorticity analysis revealed that fluid elements rotate along the surface with a strength proportional to the local curvature.

As a final note, while this study confirms the effectiveness of low-momentum burst-modulated control schemes, consistent with prior findings such as those by Amitay & Glezer (2002*a*) and Palumbo *et al.* (2022). The results also indicate that flow reattachment over an aerofoil becomes increasingly sensitive to the momentum coefficient at higher angles of attack, where substantial differences in boundary layer thickness were observed between high- and low-momentum cases. Therefore, the operational range of the control system should be carefully considered to ensure optimal performance.

Funding. The authors appreciate the support of the Natural Sciences and Engineering Research Council of Canada (NSERC) and the University of Toronto (RGPIN-2022-03071). They also thank the University of Toronto Libraries and the Canadian Knowledge Research Network for generously covering the open access fees. The third author further acknowledges support from the NOVA grant provided by Fonds de recherche du Québec (2023-NOVA-327399) and NSERC (ALLRP 577127-22).

Declaration of interests. The authors declare no conflict of interests that could have influenced the work reported in this paper.

References

ALCARAZ, E., CHARNAY, G. & MATHIEU, J. 1977 Measurements in a wall jet over a convex surface. *Phys. Fluids* **20** (2), 203–210.

AMITAY, M. & GLEZER, A. 2002*a* Controlled transients of flow reattachment over stalled airfoils. *Intl J. Heat Fluid Flow* **23** (5), 690–699.

AMITAY, M. & GLEZER, A. 2002*b* Role of actuation frequency in controlled flow reattachment over a stalled airfoil. *AIAA J.* **40** (2), 209–216.

BANYASSADY, R. & PIOMELLI, U. 2014 Turbulent plane wall jets over smooth and rough surfaces. *J. Turbul.* **15** (3), 186–207.

BARENBLATT, G.I. 1993 Scaling laws for fully developed turbulent shear flows. Part 1. Basic hypotheses and analysis. *J. Fluid Mech.* **248**, 513–520.

BARENBLATT, G.I., CHORIN, AJ. & PROSTOKISHIN, VM. 2005 The turbulent wall jet: a triple-layered structure and incomplete similarity. *Proc. Natl Acad. Sci.* **102** (25), 8850–8853.

CARMICHAEL, B.H. 1981 Low Reynolds number airfoil survey, Tech. Rep. NASA-CR-165803-VOL-1

CATER, J.E. & SORIA, J. 2002 The evolution of round zero-net-mass-flux jets. *J. Fluid Mech.* **472**, 167–200.

COLES, D. 1956 The law of the wake in the turbulent boundary layer. *J. Fluid Mech.* **1** (2), 191–226.

CULLEN, L., HAN, G., DE ZHOU, M. & WYGNANSKI, I. 2002 *The role of longitudial vortices in turbulent flow over a curved surface*, pp. 2828.

DAKOS, T., VERRIOPOULOS, C.A. & GIBSON, M.M. 1984 Turbulent flow with heat transfer in plane and curved wall jets. *J. Fluid Mech.* **145**, 339–360.

DANON, R., GREGORY, J.W. & GREENBLATT, D. 2016 Transient wall-jet flowing over a circular cylinder. *Exp. Fluids* **57**, 1–14.

DEAN, W.R. 1927 Note on the motion of fluid in a curved pipe. *Lond., Edinburgh, Dublin Phil. Mag. J. Sci.* **4** (20), 208–223.

DJENIDI, L. & AGRAWAL, A. 2024 Reappraisal of plane wall jet self-similarity. *Phys. Fluids* **36** (4), 045126.

FEERO, M.A. 2018 Investigation of synthetic jet flow control parameters for the mitigation of laminar boundary layer separation. Phd thesis, University of Toronto, Toronto, CA.

FLATT, J. 1961 *The history of boundary layer control research in the United States of America*. Pergamon.

GEE, M.T. & BRADSHAW, P. 1960 Turbulent wall jets with and without external stream. Ministry of Aviation Aeronautical Research Council Reports and Memoranda (3252).

GEORGE, W.K., ABRAHAMSSON, H., ERIKSSON, J., KARLSSON, R.I., LÖFDAHL, L. & WOSNIK, M. 2000 A similarity theory for the turbulent plane wall jet without external stream. *J. Fluid Mech.* **425**, 367–411.

GLAUERT, M.B. 1956 The wall jet. *J. Fluid Mech.* **1** (6), 625–643.

GLEZER, A. & AMITAY, M. 2002 Synthetic jets. *Annu. Rev. Fluid Mech.* **34** (1), 503–529.

GLEZER, A., AMITAY, M. & HONOHAN, A.M. 2005 Aspects of low- and high-frequency actuation for aerodynamic flow control. *AIAA J.* **43** (7), 1501–1511.

GOODFELLOW, S.D., YARUSEVYCH, S. & SULLIVAN, P.E. 2013 Momentum coefficient as a parameter for aerodynamic flow control with synthetic jets. *AIAA J.* **51** (3), 623–631.

GRATTON, J. 1991 Similarity and self similarity in fluid dynamics. *Fundament. Cosmic Phys.* **15**, 1–106.

GREENBLATT, D. & WYGNANSKI, I.J. 2000 The control of flow separation by periodic excitation. *Prog. Aerosp. Sci.* **36** (7), 487–545.

GAD-EL HAK, M. 2000 *Flow Control: Passive, Active, and Reactive Flow Management*. Cambridge University Press.

GAD-EL HAK, M. & BUSHNELL, D.M. 1991 Separation control: review. *J. Fluids Engng* **113** (1), 5–30.

HAO, M. & DI MARE, L. 2023 Scaling and similarity laws in three-dimensional wall jets. *Phys. Fluids* **35** (7), 075102.

HODSON, H.P. & HOWELL, R.J. 2005 Bladerow interactions, transition, and high-lift aerofoils in low-pressure turbines. *Annu. Rev. Fluid Mech.* **37** (1), 71–98.

HUSSAIN, A.K.M.F. & REYNOLDS, W.C. 1970 The mechanics of an organized wave in turbulent shear flow. *J. Fluid Mech.* **41** (2), 241–258.

HUSSEIN, H.J., CAPP, S.P. & GEORGE, W.K. 1994 Velocity measurements in a high-Reynolds-number, momentum-conserving, axisymmetric, turbulent jet. *J. Fluid Mech.* **258**, 31–75.

JOSHI, H. & TUMIN, A. 2004 *Centrifugal instability in a turbulent wall jet over a circular cylinder*, 1108.

VON KÁRMÁN, T. 1930 Mechanische aenlichkeit und turbulenz. In *Nachrichten von der Gesellschaft der Wissenschaften zu Göttingen, Mathematisch-Physikalische Klasse*, pp. 58–76.

LAUNDER, B.E. & RODI, W. 1983 The turbulent wall jet measurements and modeling. *Annu. Rev. Fluid Mech.* **15** (1), 429–459.

LIKHACHEV, O., NEUENDORF, R. & WYGNANSKI, I. 2001 On streamwise vortices in a turbulent wall jet that flows over a convex surface. *Phys. Fluids* **13** (6), 1822–1825.

LISSAMAN, P.B.S. 1983 Low-Reynolds-number airfoils. *Annu. Rev. Fluid Mech.* **15** (1), 223–239.

MILLIKAN, C.B. 1938 A critical discussion of turbulent flows in channels and circular tubes. In *Proceedings of the Fifth International Congress for Applied Mechanics*, pp. 386–392.

NAQAVI, I.Z., TYACKE, J.C. & TUCKER, P.G. 2018 Direct numerical simulation of am wall jet: flow physics. *J. Fluid Mech.* **852**, 507–542.

NEUENDORF, R. & WYGNANSKI, I. 1999 On a turbulent wall jet flowing over a circular cylinder. *J. Fluid Mech.* **381**, 1–25.

PALUMBO, A., SEMERARO, O., ROBINET, J.-C. & DE LUCA, L. 2022 Boundary layer transition induced by low-speed synthetic jets. *Phys. Fluids* **34** (12), 124113.

PANCHAPAKESAN, N.R. & LUMLEY, J.L. 1993 Turbulence measurements in axisymmetric jets of air and helium. Part 1. Air jet. *J. Fluid Mech.* **246**, 197–223.

PRANDTL, L. 1925 Bericht über die entstehung der turbulenz. *Zeitschrift für Angewandte Mathematik Und Mechanik* **5**, 136–139.

RAYLEIGH, L. 1916 On the dynamics of revolving fluids. *Proc. R. Soc. Lond. Ser. A* **93** (648), 148–154.

RODI, W. 1975 A new method of analysing hot-wire signals in highly turbulent flow, and its evaluation in a round jet. *Disa Information* **17**, 9–18.

SAHNI, O., WOOD, J., JANSEN, K.E. & AMITAY, M. 2011 Three-dimensional interactions between a finite-span synthetic jet and a crossflow. *J. Fluid Mech.* **671**, 254–287.

SAVALIYA, S.B., KUMAR, S.P. & MITTAL, S. 2010 Laminar separation bubble on an Eppler 61 airfoil. *Intl J. Numer. Meth. Flow* **64** (6), 627–652.

SCHARNOWSKI, S., BROSS, M. & KÄHLER, C.J. 2019 Accurate turbulence level estimations using PIV/PTV. *Exp. Fluids* **60** (1), 1–12.

SHKARAYEV, S.V., IFJU, P.G., KELLOGG, J.C. & MUELLER, T.J. 2007 *Introduction to the Design of Fixed-Wing Micro Air Vehicles Including Three Case Studies*. American Institute of Aeronautics and Astronautics.

SHUSTER, J.M. & SMITH, D.R. 2007 Experimental study of the formation and scaling of a round synthetic jet. *Phys. Fluids* **19** (4), 045109.

SMITH, B. & GLEZER, A. 1997 *Vectoring and Small-Scale Motions Effected in Free Shear Flows Using Synthetic Jet Actuators*, pp. 213. AIAA.

SMITH, B. & SWIFT, G. 2001 *Synthetic Jets at Large Reynolds Number and Comparison to Continuous Jets*, pp. AIAA, p. 3030.

SMITH, B.L. & GLEZER, A. 1998 The formation and evolution of synthetic jets. *Phys. Fluids* **10** (9), 2281–2297.

WINSLOW, J., OTSUKA, H., GOVINDARAJAN, B. & CHOPRA, I. 2018 Basic understanding of airfoil characteristics at low Reynolds numbers (10^4–10^5). *J. Aircr.* **55** (3), 1050–1061.

WYGNANSKI, I. & FIEDLER, H. 1969 Some measurements in the self-preserving jet. *J. Fluid Mech.* **38** (3), 577–612.

WYGNANSKI, I., KATZ, Y. & HOREV, E. 1992 On the applicability of various scaling laws to the turbulent wall jet. *J. Fluid Mech.* **234**, 669–690.

XU, K. 2025 Separation control on a NACA, 0025 airfoil wing using an array of synthetic jets. Phd thesis, University of Toronto Institute for Aerospace Studies. Toronto, CA.

YANG, Z. & HU, H. 2008 Laminar flow separation and transition on a low-reynolds-number airfoil. *J. Aircr.* **45** (3), 1067–1070.

YARUSEVYCH, S., SULLIVAN, P.E. & KAWALL, J.G. 2009 On vortex shedding from an airfoil in low-Reynolds-number flows. *J. Fluid Mech.* **632**, 245–271.

ZHONG, S., JABBAL, M., TANG, H., GARCILLAN, L., GUO, F., WOOD, N. & WARSOP, C. 2007 Towards the design of synthetic-jet actuators for full-scale flight conditions: Part 1: the fluid mechanics of synthetic-jet actuators. *Flow, Turbul. Combust.* **78** (3), 283–307.